# UNIVERSITÀ DEGLI STUDI FIRENZE

# Aeromechanical characterization strategy for high pressure steam turbines

Settore scientifico disciplinare ING-IND/08

**Dottorando**
Dott. Peruzzi Lorenzo

**Tutor**
Prof. Andrea Arnone

**Coordinatore**
Prof. Maurizio De Lucia

*Firenze, 2014/2017*

# Aeromechanical characterization strategy for high pressure steam turbines

Settore scientifico disciplinare ING-IND/08

**Dottorando**
Ing. Lorenzo Peruzzi

**Tutor**
Prof. Ing. Andrea Arnone
*Dept. of Industrial Engineering*
*University of Florence*

**Co-tutor**

Dr. Ing. Lorenzo Arcangeli
*Baker Hughes, a GE company*

Dr. Ing. Lorenzo Pinelli
Dr. Ing. Juri Bellucci
*Dept. of Industrial Engineering*
*University of Florence*

# Acknowledgements

First of all, I wish to express my gratitude to Prof. Eng. Andrea Arnone for giving me the opportunity to serenely pursue my PhD activity within his research group.

A special thanks goes to Eng. Lorenzo Arcangeli from BHGE and his team for the close cooperation and the interest shown for my activity in all these three years.
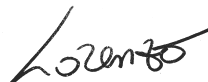
An heartfelt thank to all the colleagues (and friends!) of the T-group for the advices received but especially for the countless pleasant moments together; the mood in our office is really fantastic and it was certainly one of the ingredients that made this experience really special!

Among the colleagues of the office a special thanks must go to Eng. Lorenzo Pinelli and Eng. Juri Bellucci, which during my PhD activity have been both my *"Sensei"*: Lorenzo for having guided me, trained and given me the means to juggle in the research activity and not least, helping me in the closing phase of the doctorate, and to Juri, for the precious support received and for have given me the opportunity to look beyond the aeroelasticity.

As *"dean of the PhD students"*, how could I not thank the other guys, whom I shared joys and bitterness of this experience and who have jokingly invested me with this honorary title, as I was the older student in the office.

Thanks also to my friends, both those historical, both those acquired during the years; I have always feel them closer to me.

But the biggest thanks anyway goes to my family, to whom I dedicate every single effort made to goal this result.

*Lorenzo*

*"If you want to find the secrets of the universe,
think in terms of energy, frequency and vibration"*

**- Nikola Tesla**

# Contents

# List of Figures

# Nomenclature

**Latin**

$[\Lambda]$      Generalized damping matrix for dynamic equation

$[K]$      Generalized stiffness matrix for dynamic equation

$[M]$      Generalized mass matrix for dynamic equation

$\mathcal{L}$      Aerodynamic work

$\underline{F}(t)$      Generalized forcing vector

$\underline{x}$      Generalized displacements vector

$\vec{c}$      Blade surface velocity

$\vec{f}$      Body forces

$\vec{n}$      Blade surface normal vector

$\vec{u}$      Flow velocity

$A_0, A_n, B_n$      Fourier coefficient for phase lag formulation

$h_t$      Specific total enthalpy

$k$        Turbulence model, turbulent kinetic energy

$K_t$      Thermal conductibility

$m$       Aeroelasticity, modal mass

$m_{amp}$  Aeroelasticity, modal amplitude

$n_d$      Nodal diameter

$p$       Pressure

$P_k$      Turbulence model, Production term

$Pr$     Prandtl number

$Q3D$   Quasi-3D

$T$       Vibration period

$t$       Time

**Greek**

$\delta$       Logarithmic decrement

$\mu$       Viscosity

$\mu_l$      Laminar viscosity

$\mu_t$      Turbulent eddy viscosity

$\nabla$      Differential operator

$\omega$      Aeroelasticity, vibration pulsation

$\omega$      Turbulence model, Kinetic energy dissipation rate

$\rho$       Density

$\tau_{ij}$     Stress tensor

$\vec{\varphi}$      Heat flux density

$\vec{\vec{\sigma}}$      Viscous stress tensor

$\xi$     Energetic damping coefficient

$d\Sigma$     Infinitesimal blade surface

**Acronyms**

BC's     Boundary Conditions

BPF     Blade Passing Frequency

CFD     Computational Fluid Dynamics

CSD     Computational Structural Dynamics

DFT     Discrete Fourier Transform

DOF     Degree Of Freedom

FE     Finite Element

FEM     Finite Element Method

HCF     High Cycle Fatigue

HPC     High High Performance Computing

HPT     High Pressure Turbine

HRN     High Reynolds Number

IBPA     InterBlade Phase Angle

LCF     Low Cycle Fatigue

LE     Leading Edge

LPT     Low Pressure Turbine

LRN     Low Reynolds Number

MDOF  Multiple Degree Of Freedom

MPI     Message Passing Interface

PS     Pressure Side

RANS   Reynolds Averaged Navier–Stokes

SDOF   Single Degree Of Freedom

SS        Suction Side

TE        Trailing Edge

URANS   Unsteady Reynolds Averaged Navier–Stokes

# Abstract

The aim of thesis is to identify a viable strategy for the aeromechanical characterization of high pressure steam turbine stages. The aeromechanical characterization is focused on two main aspects: on the one hand, the evaluation of the blade damping behaviour, on the other hand, the study of forcing effects coming from neighbour rows interaction.

A possible exploitation of the aeroelasticity phenomena to increase the damping behaviour of a row, is possible thanks to the know-how gained in years with the study of the LPT flutter. In doing so, numerical methods already developed can be applied to compute the energetic damping coefficient provided of HPT rotor blades and the damping value can be further used as design parameter of these geometries, in order to improve their dynamic behaviors. The other part of this work concerns the study of the interactions between adjacent rows, which is nowadays a well-know area of interest in turbomachinery field. The goal of this activity is to investigate the tangible effect on unsteady blade loading on issues related to the HCF residual life decreasing when resonance phenomenas arise.

To meet all these purposes, the first part of this work have been dedicated to the FEM modelling of the blades with open source tools in order to obtain the row mode-shapes, which will be imposed on aerodynamic surfaces of blades for flutter computations.

Lather, the focus of the work is moved to the research for the best setup of the CFD computations to reduce the computational time without decreasing the result accuracy. Once the best setup was found, the aeroelastic computations are carried out and the results presented in term of logarithmic decrement curves for the first 4 modeshape family. The trend of the curves will be critically discussed in order to have a deep insight into the damping behaviour of these rotor blades.

As far as forcing on blade is concerned, the stator-rotor-stator interactions are studied in order to capture the unsteadiness effects on the blade loading. Thanks to the DFT spectrum of unsteady blade loads the main sources of forcing on rotor are identified and to pinpoint the unsteady contents of the fundamental harmonics, an acoustics discussion on the result is performed following Tyler and Sofrin theory.

As final part of the work, the effects of the multirow environment on the rotor damping behaviour are quantified by means of a 1.5 stage unsteady computations with vibrating rotor. The scope of this unconventional and demanding computation is to verify and endorse the single blade classical approach used for aerodynamic damping evaluation.

# Thesis objectives and outline

## Objectives

The main objective of this thesis is to identify a numerical strategy for the aeromechanical characterization for a high pressure steam turbine blades, that can be integrated with classical mechanical and aerodynamic criteria already used in the current industrial design practices.

The novelty of this approach is represented by the possibility of exploiting the aeroelastic phenomena (that are flutter and forced response), commonly considered a negative aspect in turbomachinery field, to improve the damping behaviour of a blade row and to have a better understanding of the aerodynamic sources connected to resonance effects.

To meet these purposes this procedure must be of general application for HP stages, in order to minimize uncertainness and computational tuning effort when the geometry is changed, keeping in mind that industrial procedures timing are usually tight, so the results must obtained quickly.

For the aeromechanical characterization, the aspects considered of primary importance are:

- To evaluate the aerodynamic damping contributions of a vibrating blade

- To pinpoint what are the possible sources (and their magnitude) of aerodynamic unsteady forces for the blade under investigation

- To confirm the numerical approach used for aeroelastic computation in a more realistic multirow CFD domain

## Aerodynamic damping evaluation

In order to asses the damping contribution of the blade related to the aerodynamic, an uncoupled method is adopted; the blade modeshape are computed using a open source FEM solver (CalculiX) and the results are compared with the ones coming from an widely used commercial code to confirm the goodness of the obtained results; at the same time, the best CFD calculation setup is identified to obtain confident results in term of blade loading.

Aeroelastic computations will be carried out for several modeshape families, checking the results coming from both full/simplified setup. Due to the high modal frequency of this kind of geometry, the obtained results are widely investigated to have a deep insight of the modal response.

## Aerodynamic forcing effect

In this part of work, the subjects of the research activity are the forcing effects due to the aerodynamic interactions between adjacent rows. Multistage unsteady computations are carried out using an in-house CFD code (Traf) to solve the unsteady pressure field acting on the blade row.

The spectral contents of the unsteady forces is used to identify the main frequencies of excitation and a simplified acoustic analyses was carried out to better understand the forcing phenomena.

These information can be usefully exploit in the design chain of the blade for dynamic response analyses.

## Multistage aeroelastic computations

In the final part of the work, a novel numerical approach to asses aeroelastic stability is presented. The multirow flutter analyses were carried out in a 1.5 stage domain comprehensive of two stators and one vibrating rotor.

These type of computations are particularly demanding in term of computational time and CPU power and the numerical setup shows some critical aspects. Anyway this approach represents a validation of the classical method used in the first part of the work where a single row environment was adopted.
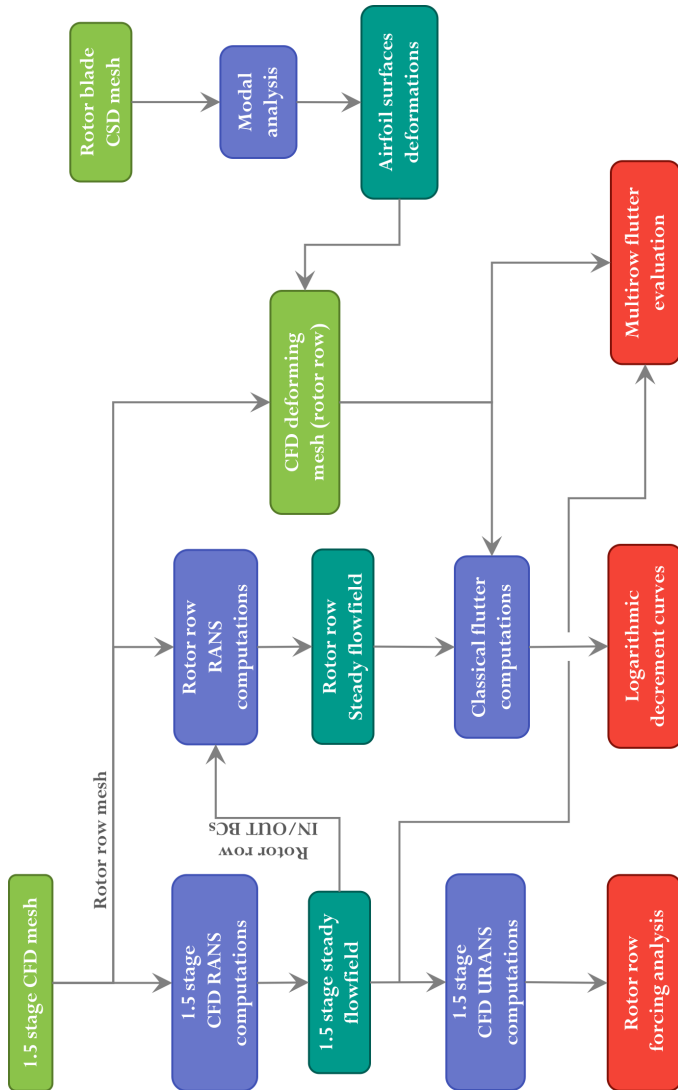
**Aeromechanical charaterization procedure overview**

# Outline

One of the main aim of this thesis is to highlight as the aeroelastic phenomena, commonly considered detrimental in turbomachinery field, can be usefully exploited to improve the vibration damping of a blade rows.

This procedure will be integrated in the industrial design practices together with the classical used mechanical and aerodynamic criteria. For this reason, the main topics of the thesis is to trace a robust, general and feasible (for the timetable of the industrial design framework) method to include these further aspect in the aeromechanical design loop. To do this, the outline of the thesis is as follows:

In **chapter 1** the overall framework of this thesis is presented. First of all, the main aspects of the typical three dimensional flow in a common high pressure steam turbine stage are presented together with a wide overview on the most relevant sources of aeromechanical forcing. In the final part of the chapter, the state of the art for current aeroelastic computations will be presented.

In **chapter 2** both flutter and forced response aeroelastic phenomena are discussed with a particular emphasis on the triggering sources. Moreover, an overview of the numerical methods available in the literature for aeroelastic computations is presented.

The numerical method used for all the flutter computations is presented in **chapter 3** with a discussion about the in-house CFD code and its validations for aeroelastic purposes. An important aspect of the code that is the treatment of circumferential boundary conditions used for single blade computations is here discussed.

The **chapter 4** describes the blade geometry and the finite element model used to perform modal analysis. The blade modeshapes coming from modal analyses are used to

deform the CFD grid for unsteady computations. The modal results obtained with a commercial code are also compared with the ones coming from a free CSD solver. The last part of the chapter is focused on the discussion of modal analysis results.

In **chapter 5** the analyzed steam turbine stage layout is described and the best CFD setup in term of computational time/accuracy is shown.

In **chapter 6** are illustrated the results obtained from classical single-row flutter computations to evaluate the aero-damping of the rotor. Some important modal aspects typical of this HP blade as the mode veering are explained in detail.

The sources of aerodynamic forcing effects due to row interactions are dealt with in **chapter 7**, where a wide discussion of the force amplitude and the generation mechanism is included.

In **chapter 8** the effects of adjacent stators on rotor damping behaviour is studied with a new multirow approach in order to verify whether the single blade computations carried out in chapter 6 are representative of the actual multi-row environment where the rotor operates.

In the **chapter 9** all the obtained results are summarized and discussed; At the end of of this work, some possibles future developments are proposed.

# 1

# Introduction

Over the last few years, the world energy landscape has been engaged by a growing demand for highly efficient turbomachineries both in the field of aeronautical propulsion and power generation. To meet this requirement, one of the strategy that has been adopted by designers is the reduction in the number and overall weight of the components, that become necessarly more loaded and slender. Even though these two aspects bring the expected achievement to an efficiency gains, from the other hand, they favor the arising of interaction phenomena between vibrating blades and the operating fluids, which could compromise structural integrity by reducing fatigue life.

The aeroelasticity, an interdisciplinary matter that involves fluid and structural dynamics, studies these interaction phenomena both from a theoretical point of view and both through the development of numerical methods with the purpose to accurately predict the intensification or damping of rowss vibrations. Nowadays, the knowledge gained over the years in aeroelastic field allows to look at these phenomena not only as an issue, but something that can even be positively exploited.

Today, steam plants still play a major role in turbomachinery field, being adaptable to a large part of the energy requirements, from large-scale plants for massive production of electricity to small-size solutions for co-generation purposes. Fatigue issues due to vibration phenomena or required plant downtime for maintenance, translate in high direct and indirect costs. Indeed, it is clear that the knowledge of the row aeroelastic behavior from the starting project phases, becomes necessary for a proper blade aeromechanics design, in order to achieve an "infinite life design".

## 1.1 Background

Typically, due to high temperature and density, the flow inside the high-pressure steam turbine stages does not exhibits issues related to complex structures of motion like shocks waves or real gas effects (nucleation of water drops, compressibility effects related to less than one quality of the steam).

The steam, after having evolved through the first control stages, passes through a series of reaction stages working with similar flow configurations, in a condition usually referred to as "repeating stages". In this panorama, the CFD steady flow analyses can profitably used to describe the stages flow and to capture all the aspects linked to performance and losses. However, looking towards the study of the fluid/structure interactions, the intrinsically unsteady nature of the flow due to the stator/rotor interactions cannot be ignored. These effects are well know as the main sources of aerodynamic forcing capable to reduce the life of the rows due to the occurrence of HCF problems.

Even if the designers strive to reduce vibration amplitude, due to the innate elastic character of the blades, vibration cannot be completely suppressed. Sometimes the interaction between the flow field around the blade and its modeshapes is translated into the onset of aerodynamic instability phenomena called "Flutter" which bring to an amplification of the vibrations causing high mechanical stress (and therefore

reduced fatigue life). Due to their inertial and elastic common features, flutter failures are unusual for HP stages where the aerodynamic constraints are enough to ensure a resulting flutter-free geometry despite the few aeroelastic investigation of this type of stage. In any case, even through instability phenomena are usually not present, an high interaction between fluid and blade occur; the effect of a flutter-free interaction is energy flux from the blade to the fluid with a macroscopic effects of the vibration damping.

This positive effects coming from the aeroelastic interaction can be positively exploited as additional damping introducing a energetic damping coefficient to estimate the mutual interaction between dynamic and aerodynamic effects. This quantity, usually employed to asses flutter instabilities, in this case of high stability may also be used as a further damping effect similar to the ones provided by frictional or interfering damping devices usually mounted at interface of adjacent blades to introduce mechanical damping.

## 1.2  Flow in HP steam turbines

To clearly describe the main characteristics of the flow and to have a wide overview on the HP stage aerodynamics, it is useful to briefly recall some fundamental concepts.

Typically, even if CFD steady flow analyses are able to correctly describe and predict the overall machines performance, the flow inside the turbine rows is inherently unsteady, due to stators and rotors rows in relative motion and so upstream and downstream interactions occur. Even looking inside a single row, just for the interactions of the flow with high deflection blade airfoils, unsteadiness may be detected.

All these flow features have a deep impact on turbomachinery performances as stage efficiency, blade loading, mechanical and thermal fatigue resistance, heat transfer, and noise low generation.

Among the dedicated literature, narrowing it down to the ones on interest for this work, is is possible to identify some aspects that can influence blade loading that are:

- Secondary flows

- Potential effect

- Impingement of upstream wakes

### 1.2.1    Secondary flow

According to Lakshminarayana in [4], secondary flows are all that which are different from the main reference flows, or in a more rigorous way, a secondary flow is what is generated by the vorticity component along streamlines.

Due to high deflections of the main flow in a turbine channel and the thick leading edge of a typical HP turbine blade, the secondary flows in turbine rows are generally more complex compared with compressors environment, so, to well understand their characteristic, it can be helpful referring to the exhaustive work by Sieverding in [5], and Takeishi et al. in [6].

In figure 1.1, a magnified representation of turbine endwall secondary flows is reported, where it can be seen as the flow field near the hub endwall region of the blade passage is dominated by the presence of boundary layer, strong pressure gradients, and cross flow in the pitchwise direction.

The horseshoe vortex is generated by the rolling up of the boundary layer at the blade LE in the blade/endwall junction region.

The main flow results "splitted" into two structures which evolves on the blade surfaces, usually referred to as *pressure side leg* and *suction side leg* of the horseshoe vortex. Due to the streamlines curvature, the flow is driven in a pitchwise motion with an endwall crossflow resulting in a development of a new boundary layer on the endwall.

The two legs of the horseshoe vortex are convected downstream and due to their pitchwise motion, the pressure side

leg vortex of a blade merges with the suction side leg vortex of the neighborhood blade in a stronger vortex known as the *passage vortex.*

Since the pressure gradients in large deflections blade can be very strong, the secondary flows can be so intense to considerably modify the aerodynamics of the row in the close to endwalls regions [7].
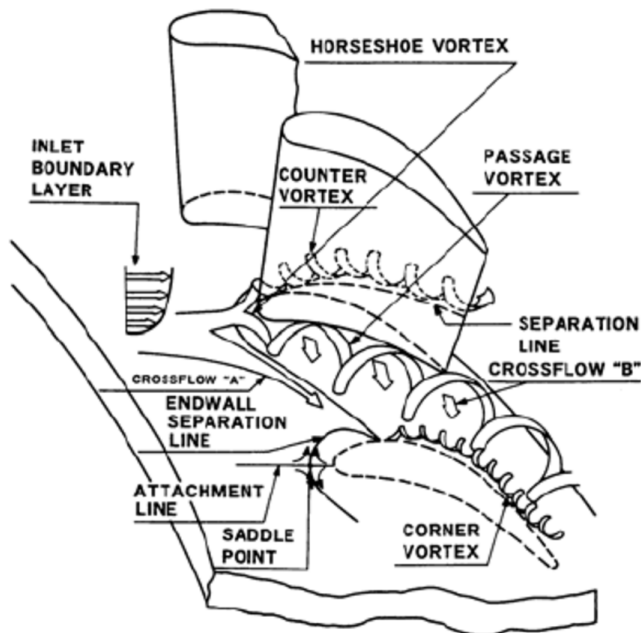


**Figure 1.1:** Endwalls secondary flow model for turbine blade [6]

During years many experiments and correlation has been developed in order to capture the effect of the shape of the blade on the secondary flows growth; from a review of the literature ([8], [9], [10]) emerges the well-known correlation between the blade aspect-ratio and secondary flow losses,

highlighting a reduced effect of secondary flow for blade with higher aspect-ratio [11] as can be seen in figure 1.2.
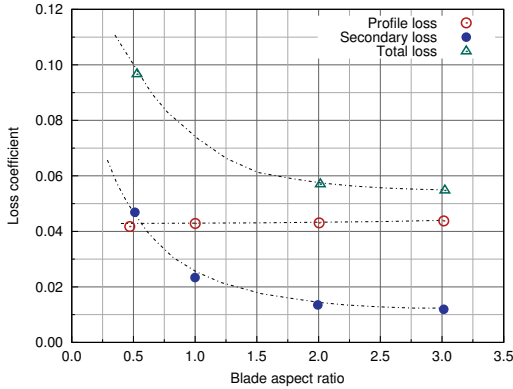


**Figure 1.2:** Aspect ratio Vs. Loss coefficient (replot from [11])

To ensure that the stage works at the design point in the peak efficiency region of the Smith chart, here reported in figure 1.3 ([12], [13]), the designers tend to position the blades far from the machine axis in order to reduce the radius ratio of the stage and consequently relieve the effects liked to three-dimensional flows.

The design of the stage is in fact a compromise between aerodynamic and mechanical needs that for high pressure stages lead to high blade counts and blades with high aspect ratios (generally around 3.0) to confine the secondary flows to the endwall regions lowering their effects on the average aerodynamics of the stage.

## 1.2.2   Rows potential interaction

The working fluid in turbomachinery due to its viscosity is inherently rotational, and then, the interaction between the velocity field and the channel surfaces is a source of circulation.
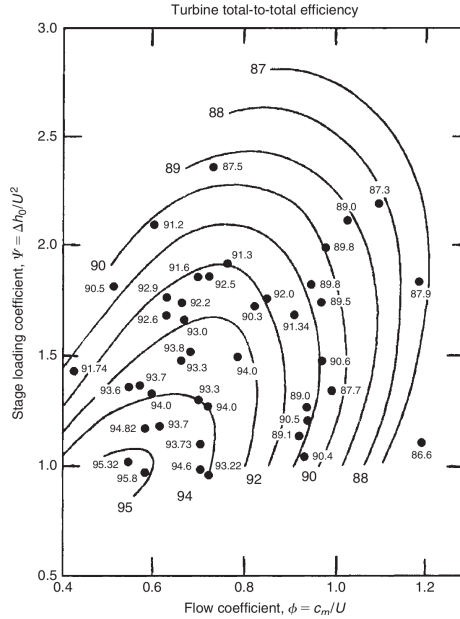
**Figure 1.3:** Smith chart

The circulation around a blade creates a potential field and non-uniformities in static pressure distribution at the inlet or outlet plane. These non-uniformities propagate through the flowpath and when one blade row is moving relatively to the successive ones, the potential field interacts with the other blades resulting in a distortion in pressure and velocity fields. The magnitude of this effect depends on a number of factors as stated by Parker and Watson in [14] and Osborne in [15]. In a subsonic flow (M<1.0) the potential field associated with a blade row propagates both upstream and downstream from the blade, decaying proportionally to the relation in 1.1.

$$e^{-2\pi\sqrt{1-M^2}\frac{x}{p}} \tag{1.1}$$

where $M$ is the Mach number, $x$ the axial distance from the rows and $p$ is the row pitch.

This equation is valid only as a first approximation as it is coming from a simplification of the physics of the interaction based on the propagation of acoustic waves in purely axial flows (not so realistic for a cambered airfoil used in turbines).

It states that in low subsonic flows, potential disturbances decay in the axial direction, and Parker and Watson in [14] suggested that the effects of potential interactions can be neglected if the axial spacing is greater than about 30% of the blade pitch, while near to sonic conditions they propagate almost unattenuated.

From aeromechanical point of view, the relevance of the potential interactions is related to a periodic changes in flow incidence with blade passing frequency and its harmonics, and then results in an unsteady blade loading, capable to trigger forced response phenomena.

In the stage under investigation, the flow is subsonic, but the neighborhood rows are closer than advised in [14] to achieve an sufficient decays of potential interaction and then potential effect interaction cannot be neglected.

### 1.2.3   Wakes impingement

As shown in figure 1.4, the boundary layers after leaving the trailing edges of the blades, on both pressure and suction surfaces develop into a wake convected downstream ([16]).
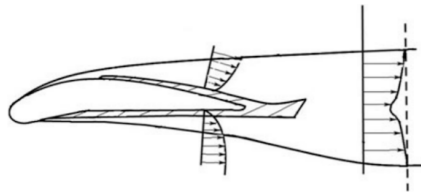


**Figure 1.4:** Wake develop

The wakes coming from the upstream rows impinge on the downstream row and it is characterized by different components in term of entropy and vorticity respect to the main

flow. These different properties of the fluid inside/outside the wakes produce a different incidence on the following row due to the alteration of triangle of velocity as shown in figure 1.5.

This change in incidence is less problematic in turbine rows rather than compressor rows due to the thick leading edge, but it produces anyway fluctuating lift and drag forces on the following blade rows when the wake passes and contributes to the overall unsteadiness of the stage.
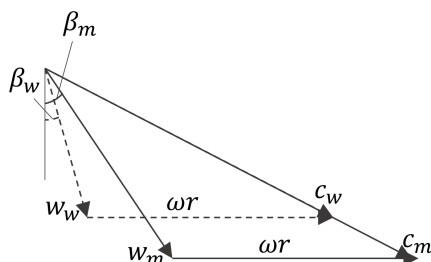


**Figure 1.5:** Wake/main flow velocity triangle

The effect of the wake presence is not limited to a change of incidence; incoming velocity defect approaching the blade is "chopped" into independent segments convected downstream in the vane where is commonly treated as a negative jet as shown in figure 1.6. Due to the pressure gradients inside the negative jet, the fluid is "pumped" from pressure to suction side of the vane and affect the blade distribution of unsteady pressure, and thus blade loading.

Inside the vane, the wake segment is distorted as the main flow in the center of the vane moves faster than near the blade surfaces. When the wake enters inside the row vanes, the local velocity stretch the segment in a arc-shape (this phase is called *wake bowing*); later due to higher velocity on the suction side respect to the pressure side, the wake segment is deformed again from the arc shape into a flow-oriented zone practically parallel to pressure surface with a mechanism called *wake reorientation* [16].
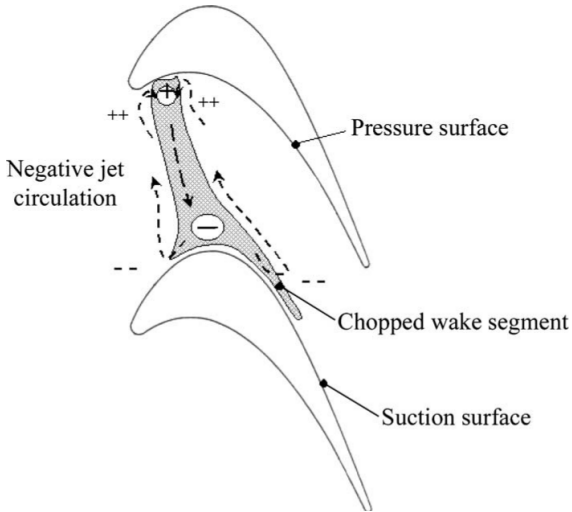
**Figure 1.6:** Negative jet in turbine a row

## 1.3    Past effort and state of the art

The idea of this work is to numerically compute the unsteady response of the flow around a vibrating row (responsible for the aerodynamic damping) with the methodologies mainly developed to assess the stability of stages more prone to flutter issues and to quantify the damping effect of the blade/fluid interaction adding this information in the common dynamic analyses of the row. The first aeroelastic numerical methods, developed at the beginning of the 1970s, were based on linear approaches where all the equations are linearized [17, 18].

Since the 1990s, time-linearized methods have been developed: according to these approaches, the flow is decomposed into a non-linear steady flow plus a small-perturbation harmonic unsteady flow [19, 20, 21, 22, 23, 24].

In recent years thanks to the growth in computer technology, non-linear methods have become a viable alternative

and several non-linear (uncoupled and coupled with structural solver) approaches have been implemented [21, 25, 26, 27, 28, 29, 1, 30]. In particular in decoupled systems, structural modes and frequencies and unsteady blade row interaction forces and aeroelastic forces are calculated separately due to is usually accepted that modeshapes remain unaffected by the surrounding fluid.

In order to accurately simulate the actual characteristics of a row, taking into account both structural and dynamic aspect, and thanks to the increasing availability of computational power, many formulations of coupled methods have been proposed in weakly or strongly formulation.

In the weakly formulation, the structural dynamic and the fluid dynamic equations are solved separately as in decoupled method. The solution on one domain represents the boundary condition for the other one with an exchange of information on the solid/fluid interface (*i.e.* the blade surface) for each time step. The main issue related to this method is linked to the different computational request for solving fluid and structural domain and the time step needed to achieve the convergence. For the most time of the run, the structural solver waits for the BC's coming from fluid domain.

To go beyond these issues, the fully coupled formulation were proposed ([31, 32, 33, 34, 35]). Solid and fluid domains are no longer treated separately, but are merged into a single Lagrangian-Eulerian hybrid domain. Since there are no temporal gaps between the two solutions, these methods are more accurate in the prediction of the energy exchange between the fluid and the vibrating row.

The computational effort for this type of method becomes relevant both in time and CPU power. Moffatt and He's works study [36] study the influence of decoupled and fully coupled systems on the forced response amplitudes of a transonic fan.

From their computations is is clean that the coupled solution exhibits a significant frequency shift due to the added mass effect of the vibration-induced aerodynamic damping forces. On the other hand the decoupled ones are instead

insensitive to this frequency shift maintaining resonance at the blade natural frequency and capturing the resonant peak. Due to the practicality and thanks to the accurate predictions, decoupled methods have been currently identified as to be the best approaches for solving blade-row interaction problems and the more suitable for industrial needs.

While, on the one hand it is necessary to reduce the vibrations phenomena, on the other hand it is also important to identify the sources that may trigger row oscillation. Vibration sources in the blades are various: seal rubs, vibrations transmitted by the gearbox, effects due to rolling in the supports, yet the interactions between adjacent rows are the more relevant causes.

The distortions of the unsteady flow caused by the presence of the blades and also the acoustic interactions between the stages can be now adequately reproduced with CFD methods. Once the unsteady field is accurately resolved, aerodynamic forcing effects can be identified can be included in the mechanical design phase, avoiding possible resonances.

The aeromechanical characterization strategy proposed in this work includes solutions to aeromechanical issues and design requirements in a robust and repeatable procedure, suitable for direct application to industrial problems and ready to be included inside the actual design practices.

# 2

## Aeromechanics

*In this chapter aeroelastic phenomena will be discussed, paying attention to ones that may arise in turbomachinery field.*

*After a brief overview on aeroelastic phenomena and their fatiguing effects on blades, the state of art of computational aeroelasticity will be shown focusing to numerical methods for flutter prediction.*

## 2.1   Blade Vibration issues

The main target that designers have to follow in modern steam turbine design, is to improve the machines efficiency. The challenge to be faced with, is to combine a reduction in blades count with more loaded profiles. For this reason blades are therefore becoming more slender and loaded, with a consequent increase of aeroelastic phenomena onset that could compromise the structural integrity.

The vibratory conditions which may occur reduce blade fatigue life, leading in the worst cases to failures. Nowadays the vibration problems are mostly related to economic

factors due to scheduled maintenance plans with consequent stopovers and thus increasing indirect costs.

The knowledge gained during the years, coupled with an increasing computing powers has allowed the study of aeroelastic phenomena not only as a problematic aspect in design but also as something that can be advantageously exploited. In fact, problems related to aeroelasticity in a steam turbine mostly affect low pressure stages due to mode-shapes with low frequency, while high rigidity (and hence higher frequencies), bring high pressure stages to experience no aeroelastic issues. In this light for high pressure stages, the positive effects of fluid/structure interaction (i.e. a positive aerodamping effects), may be consider as an additional damping in addiction to the damping due to classical frictional underplatform dampers, bring towards an easier mechanical design of the blade features (roots, fillets, etc...).

## 2.2 Aeroelastic phenomena

By the term "aeroelasticity " it is common to indicate an interdisciplinary area that relates to the study of interactions between an elastic body immersed in a fluid in motion. The study of aeroelasticity involves several disciplines (see Fig. 2.1): from the dynamics of the elastic body system related to its inertial behavior, to the study of the stresses due to deformations, the effect of fluctuating pressure field acting on the body surfaces, considerations about energy-related properties linked to system damping and even heat exchange between fluid and rigid body. Even if the correct terminology would be "fluidotermoelasticity", in the field of engineering the use of the term "aeroelasticity " is more common (see [37]) to refer to this discipline.

Aeroelastic issues arise in different branch of engineering science; the most famous and well reported episode associated to a aeroelastic failure is the Tacoma-Narrow bridge collapse in civil engineering field, but other episodes are reported in
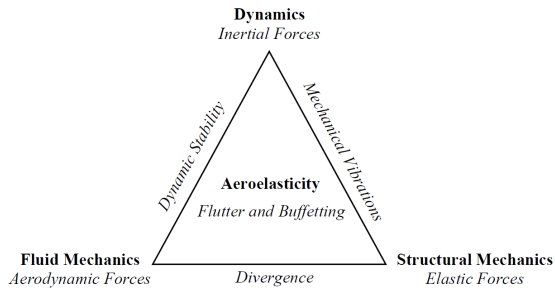
**Figure 2.1:** Collar Triangle (see [38])

aviation field where NASA detected wing and elevon flutter on military jets.



**(a)**                  **(b)**
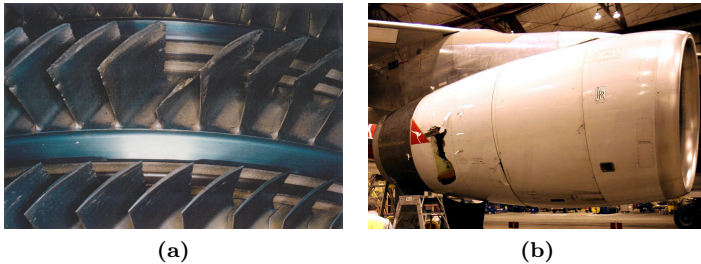
**Figure 2.2:** Aeroelastic failures effects

Related to turbomachinery field for propulsion and energy generation, in Fig. 2.2a a failure of a compressor row due to fatigue induced by flutter effects is shown, while in Fig. 2.2b it is possible to understand how severe can be the consequences of similar failures (in this case the failure clearly affect the turbine stages of turbofan).

The two more common aeroelastic phenomena that may arise in turbomachinery blade row are the "Forced Response" and "Flutter".

### 2.2.1   Forced Response

"*The forced reponse is an aeroelastic interaction which causes blade vibration induced by upstream/downstream excitations due to wakes and potential fields.*"

This is a resonant condition for the fluid/blade system, and even though the vibration is stable, its onset is always undesirable as it can affect the fatigue life of the blade.

The forced response vibration is not only due to aerodynamic effects, but also to different excitations which can be give a resonance effect can be a potential source of vibration. Commonly, the well-know source of forced vibration are:

**Gust,** a non-uniformity in flow field due to adjacent rows such as potential effects and incoming wakes

**Adimission distortion,** commonly present in the partialized stages of actions steam turbine stages

**Stall cells**  both upstream or downstream respect to the rows

**Friction rub**  in the brushing seals

**Sincronous effects**  coming from engaging in the gearbox

Historically, the forced response was the first investigated aeroelastic phenomenon (see [39]), by simply solving the system of motion dynamics $[M]\underline{\ddot{x}} + [\Lambda]\underline{\dot{x}} + [K]\underline{x} = \underline{F(t)}$.

Moreover, once the system eigenvalues are found, a Campbell diagram (as shown in the Fig. 2.3) can be traced, locating all the possible resonance occurrence by identifying the crossing between engine orders and blade natural frequencies curves.
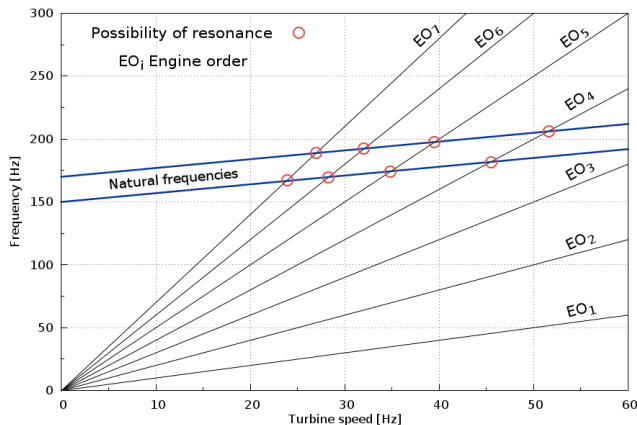
**Figure 2.3:** Campbell plot

## 2.2.2 Flutter

*"With term "Flutter" it is means a self-induced aeroelastic vibration that begins and sustains itself without any incoming upstream/downstream distortions"*

Unlike forced vibration, flutter is a condition of instability and not of resonance for the fluid+solid system. This vibration is usually triggered by a random excitation and the unsteady pressure field acting on the vibrating blade does the so-called "aerodynamic work, $\mathcal{L}$" thus defined over a vibration period T.

$$\mathcal{L} = \int_t^{t+T} \int_S (-p)\, \vec{n} \cdot \vec{c}\, d\Sigma\, dt \qquad (2.1)$$

In case of flutter, the pressure field performs a positive aerodynamic work and so the amplitude of vibration tends to increase more and more; several scenarios are possible:

**Vibration break-up:** The energy extracted from the fluid is completely dissipated by the structural damping of the blade. (Fig. 2.4a)

**Cycle limit:** The energy extracted from the fluid and the one dissipated by the structural damping balance each other, so the vibration leads to a limit cycle with constant vibration amplitude (Fig. 2.4b)

**Flutter:** Structural damping is not able to dissipate entire energy extracted from the fluid and so, the amplitude of vibration gradually increases. The residual HCF life of the blade is reduced and in some case, blade structural collapse can occur. (Fig. 2.4c)
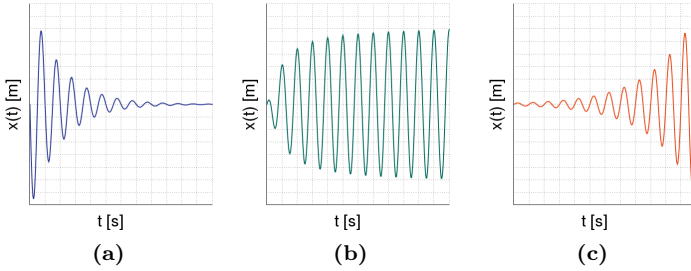


**Figure 2.4:** Possible scenarios of flutter vibration evolution

Consistent with its definitions, if $\mathcal{L}$ is negative, the energy flux direction is from the blade to the fluid and then a damping behaviour from aeroelastic effects is shown. To quantify the damping effect of $\mathcal{L}$ an energetic damping coefficient $\xi$ is defined in eq. 2.2 giving $\mathcal{L}$ non-dimensional with blade average kinetic energy. This parameter is strictly linked to the logarithmic decrement $\delta$ as shown in eq. 2.3.

$$\xi = -\frac{\mathcal{L}}{8\pi E} = -\frac{\mathcal{L}}{2\pi m \omega^2 m_{amp}^2} \tag{2.2}$$

$$\delta = 2\pi\xi \tag{2.3}$$

There are several types of aeroelastic instabilities which can be classified as flutter and usually the way to classify them, is to identify the triggering reason (see [39])

**Classical flutter,** that occurs in subsonic flows around blade with no flow separation. It is only due to interaction of aerodynamic forces on vibrating rows

**Coaleshence flutter,** is a kind of classical flutter that occurs when two natural blade frequencies of mode-shape are or very closer

**1-DOF flutter,** which occurs involving only a single mode-shape of the blade. Usually the frequency of the vibration is practically the same of the one in vacuum

**Stall flutter,** SDOF or MDOF flutter strongly non linear, that occurs in stall or stall incipient conditions of the row

**Dynamic stall flutter,** a stall flutter that onsets in only a fraction of mode-shape vibration period

**Choke flutter,** non linear kind of flutter that arises in choke or near-choke operating points

**Supersonic unstalled flutter,** a kind of flutter which exhibits all aspect of a classical flutter but occurs in supersonic unstalled flow field conditions

## 2.3 Overview of computational aeroelasticity

Numerical methods for flutter analysis are nowadays extensively used in the blade design both to predict flutter instability and flow damping behaviour. During the years several approaches to CA are developed, and as both the FE models and the CFD models are involved, the natural way of distinguish different methods is to identify how mechanical part and fluid one interact between them.

**Uncoupled approach,** where the structure vibration is assigned and only the fluid flow response is simulated, accounting for the influence of structure vibration on the

flow, but not for the opposite interaction effect. The major hypothesis of this method, is that the presence of the fluid around the blade has a negligible effect on mode-shapes, so FE modelling can be carried out in vacuuum (see [40]).

**Coupled approach** where the Navier–Stokes equations 2.4 and the motion dynamic equation 2.5 of blade are solved simultaneously, taking the mutual interaction into account with BC's exchange passage between flud and structural domain.

$$\begin{cases} \dfrac{\partial \rho}{\partial t} + \vec{\nabla} \cdot (\rho \vec{u}) = 0 \\[2mm] \dfrac{\partial (\rho \vec{u})}{\partial t} + \vec{\nabla} \cdot (\rho \vec{u} \otimes \vec{u}) = \rho \vec{f} - \vec{\nabla} p + \vec{\nabla} \cdot \vec{\vec{\sigma}}_v \\[2mm] \dfrac{\partial (\rho E_t)}{\partial t} + \vec{\nabla} \cdot (\rho h_t \vec{u}) = \rho \vec{f} \cdot \vec{u} + \vec{\nabla} \cdot \left( \vec{\vec{\sigma}}_v \vec{u} \right) - \vec{\nabla} \cdot \vec{\varphi} \end{cases} \tag{2.4}$$

$$[M]\ddot{x} + [\Lambda]\dot{x} + [K]x = F(t) \tag{2.5}$$

Several strategies of solution may be adopted for these equations:

**Linearized method** in which all equations are linearized

**Time-linearized method,** where the equations are linearized in time using the steady solution to initialize the unsteady runs with small perturbation on grid deformation ([40], [41])

**Non-linearized methods,** where the equations are directly integrated in time domain ([42], [43])

**Harmonics non-linear method,** which represents a compromise between time-linearized and non-linearized methods

In this work, an uncoupled approach with non-linear integration strategies is adopted (see chapter 3 for method explanations).

*3*

# Numerical method

*In this chapter, the numerical uncoupled aeroelastic method will be presented together with the Traf solver, used for both steady and unsteady CFD simulations. At the end of the chapter, a brief description of full annulus and phase-lagged approaches used to impose the circumferential boundary conditions for flutter computations is provided: phase lagged conditions are fundamental to reduce computational requirements.*

## 3.1 CFD solver: Traf code

All the CFD simulations have been carried out using the validated in-house Traf solver for turbomachinery flows. It is a multistage and multi-block solver for 3D/Q3D Navier-Stokes equations in RANS/URANS formulation, using the conservative form in a curvilinear, bodyfitted coordinate system (see [44], [45]). For the governing equations, the Traf code use an explicit four stage Runge-Kutta integration algorithm on a cell-centred finite volume discretization of the domain. Residual smoothing, local time-stepping, and multi-gridding are employed to speed-up convergence to the steady state solution. A dual time stepping method ([46], [47]) is

used to perform time accurate unsteady calculations. Through dual-time stepping, for every physical instant of simulation the governing equations are integrated into the pseudo-time until a threshold residual is reached while time-derivatives of the Navier-Stokes equations set are discretized using a three-point backward formula accurate in time up to second-order. Artificial dissipation model have been implemented in the Traf code in both scalar ([48]) and matrix ([49]) formulation, together with the eigenvalue scaling ([50], [51]). The most used turbulence models in turbomachinery field were implemented in the code for equations closure; from the algebraic Baldwin-Lomax model, Spalart-Allmaras one equation model and two equations $k - \omega$ model in LRN and HRN Wilcox's formulation ([52]). The code is recently parallelized for both distributed and shared memory systems, following the trend of HPC cluster architectures. The distributed memory parallelization is based on the Message Passing Interface (MPI) standard for communication, while the OpenMP standard was adopted for the shared memory parallelization. These two approaches can be independently selected or combined in a hybrid, master-only OMP-MPI parallelism at the compiling level.

The size of CFD domain is straight linked to the required computational effort in term of time and size of the solution; for the steady computations, the computational request is not so high due to a single block per rows is yet fully capable to represent the whole full-annuls mean solution thanks to the use of tangential periodicity and mixing planes. On the other hand, this setup cannot be used for unsteady simulation because the hypothesis of instantaneous tangential periodicity on domain boundaries (i.e. identical situation in time and space for all blades of a row) cannot be longer applied and then different strategies must be used for multi block or single stage simulations.

### 3.1.1   Code validation for aeroelastic analyses: review on previous works

The Traf solver, originally developed for aerodynamics purposes was extended to address flutter computations with an uncoupled non-linear method and successfully validated against experimental data.

The first validation was carried out simulating the EPFL STCF4 test case 627 ([53], [54]), which is a subsonic test case with vibrating rows for turbine blade applications.

The results are widely discuss by Pinelli et al. in [1] and they are briefly reported for the sake of completeness in this work. As show in figure 3.1a and 3.1b, the result in term of amplitude and phase of pressure perturbation coefficient obtained by the Traf code are in good agreement among different codes and well match the experimental data.
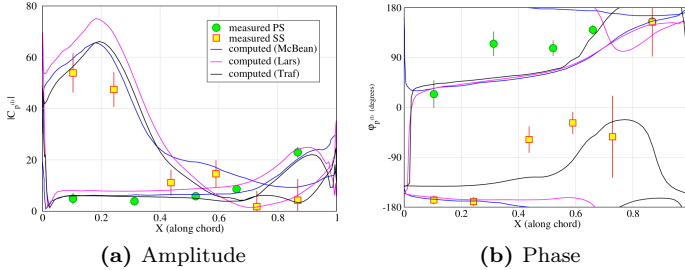


**(a)** Amplitude                    **(b)** Phase

**Figure 3.1:** Traf Vs. STCF4 Exp. results - Pressure perturbation coef. ([1])

The resulting aerodynamic damping coefficient Vs. IBPA of this testcase is reported in figure 3.3, and despite a few discrepancies, the stability range is well predicted, and the agreement with the other codes is good.

In the same paper by Pinelli et al. [1] analogous validation comparison can be found for a supersonic case (EPFL STCF4 test case 628, [53], [54]).
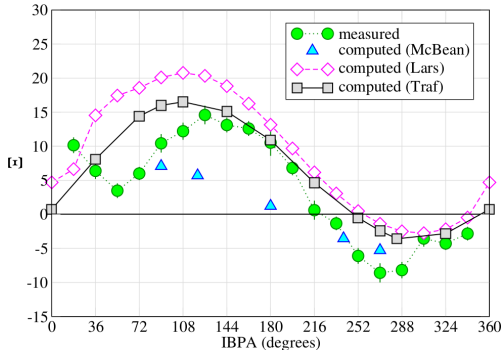
**Figure 3.2:** Traf Vs. STCF4 Exp. results ([1])

In the first extension of Traf code to flutter analyses only single blade tuned configuration with travelling wave modeshape could be simulated, later, to chase the current trend of using mistuning to suppress flutter occurrences, the solver was further extended to simulate blades mounted in packet (typically nozzles) and with different geometry. [3].

In [3], the results coming from CAE of a 4-blades cluster modeshape are compared with experimental ones coming from a dedicated test case facility (see [2]), in the context of the EU project FUTURE.

In the figures 3.4a, 3.4b, 3.4c and 3.4d the comparisons between numerical and experimental damping values shows a satisfactory agreement between experimental and numerical
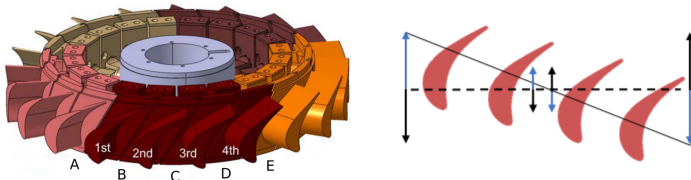


**Figure 3.3:** Traf Vs. Exp. results - Cluster modeshape facility ([2])

curves for each blades of the cluster. Due to this good matching between experimental and computed data the method can be considered validated.
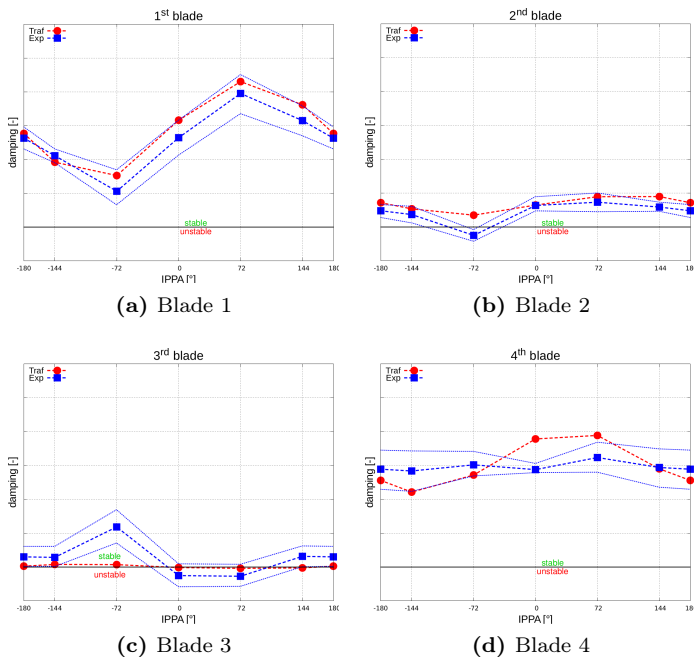


**(a)** Blade 1

**(b)** Blade 2

**(c)** Blade 3

**(d)** Blade 4

**Figure 3.4:** Traf Vs. Exp. results - 4 blade packet configuration ([3])

The stage under investigation does not exhibit cluster assembly or mistuned configuration and so, all simulation was carried out using the classical tuned blade approach, yet the results from the flutter code extension are here reported to point out all the code capabilities and suggest potential lines of development for the future works.

## 3.2 Single Blade aeroelastic computations

Looking at a typical blade rows, it is common that all blades have the same inertial, elastic and dissipative characteristics, so they vibrate within the rows with the same modeshape (tuned blades), but phase-shifted of an angle called **I**nter**B**lade **P**hase **A**ngle (IBPA) between adjacent blades. The vibration results in a deformation wave rotating in the circumferential direction along the blade row, and it is so called "traveling wave" (see chapter 4).

In this case the CFD domain must be suitable to reproduce the travelling wave; for a given nodal diameter a viable strategy can be the adoption of an adequate number of tangential vanes in order to re-obtain the instantaneous periodicity conditions on its outer tangential boundary. The pros and cons off this method is that it's very easy to adopt, but for some NDs a large number of vanes may be requested and so the computational effort becomes troublesome.
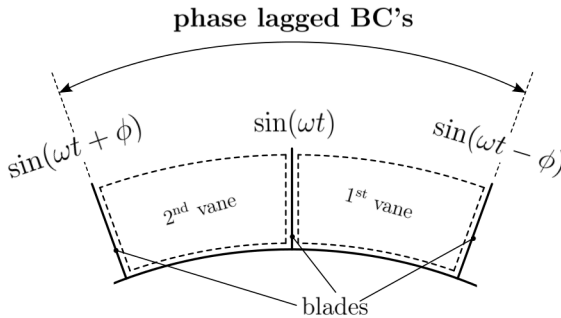


**Figure 3.5:** Chorochronic Periodicity Conditions for IBPA=$\phi$)

The travelling wave deformation implies that the conditions for one vane replay itself in the following wane with a time lag, so the use of a chorochronic formulations rather than instantaneous one for imposing tangential boundary condi-

tions allows the use of a single vane domain with all benefits in time and solution size request. This approach is implemented in Traf code (see [55]) in Gerolymos's formulation (see [56]); even if a single vane row can be sufficient to give the travelling wave, a two vanes domain is adopted to speed-up the convergence (see Fig. 3.5).

In an unsteady computation every physical quantity is time-dependent, so a generic one of it on tangential boundary may be expressed by means of Fourier series in time with a finite number of time-harmonic coefficients.

$$A_0 = \frac{1}{T} \sum_{j=1}^{NP} f(t) \Delta t$$

$$A_n = \frac{\omega}{2\pi} \sum_{j=1}^{NP} f(t) \sin(n\omega t) \Delta t$$

$$B_n = \frac{\omega}{2\pi} \sum_{j=1}^{NP} f(t) \cos(n\omega t) \Delta t$$

with $A_0$, $A_n$, $B_n$ the Fourier series constants, $n$ the harmonic index, $\omega$ and $T$ natural pulsation and period of the blade oscillation, $NP$ is the time-step number and $\Delta t$ its amplitude.

Once Fourier series coefficients are calculated for $(i)$time-step they can be used subsequently to rearrange suitable BC's through a phase lag, (straight linked to the IBPA in case of aeroelastic analysis) for the $(i+1)$time-step.

For a generic time-dependent quantity $f(t)$, according with figure 3.6, the fluid property at time $\tau^*$ can be obtained using the relations in eq. 3.1 and 3.2.

$$f_C = A_{0_2} + \sum_{n=1}^{N} A_{n_2} \sin[n(\omega t - \phi)] + \sum_{n=1}^{N} B_{n_2} \cos[n(\omega t - \phi)] \quad (3.1)$$

$$f_D = A_{0_1} + \sum_{n=1}^{N} A_{n_1} \sin[n(\omega t + \phi)] + \sum_{n=1}^{N} B_{n_1} \cos[n(\omega t + \phi)] \quad (3.2)$$

With Subscript $n_1$ e $n_2$ for $1^{st}$ and $2^{nd}$ blade. The coefficient are computed are calculated step-by-step during the vibra-

tion period and refreshed with a running average scheme to improve the convergence.
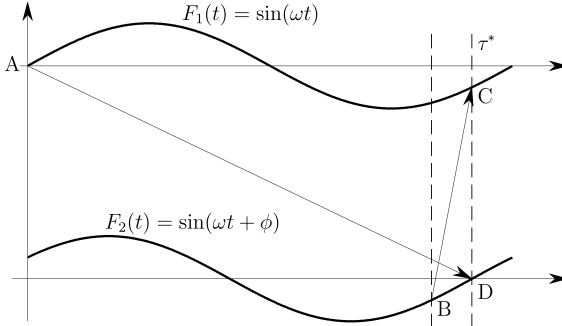


**Figure 3.6:** Determination of fluid properties through phase-lag

## 3.2.1 CSD $\Rightarrow$ CFD modeshape transfer

The method used for aeroelastic computations is an uncoupled one, so once the modal analysis is performed (see Chapter 4), the modeshapes must be transfered on the CFD grid, which is deformed in order to reproduce the travelling wave

The first issue that arise in modeshape transfer is that the CSD and CFD domains does not show the same discretization of the blade surface and so, the deformation can not be transfered node-by-node but a nearest point interpolation strategy between CSD nodes and CFD node is request.

Once the modeshapes is transfered to the CFD grid nodes of the blade surface, to follow the bladerow vibration the whole domain must be deformed. The vibration period is splitted in a finite number of equally spaced temporal step and the CFD domain rebuilt for each of it ([1]).

In this phase the sensitivity of CFD computations to shape of mesh elements (skewness, sharpness...) must be take into account so the deformation is not equally distributed over

CFD grid but the more big are elements the more is the deformation associated; following this way small elements as the one in boundary layers and around small features[1] are less deformed than the ones in the center of interblade passage vane.

## 3.3 Multirow computations

To handle multirow unsteady calculations, two different approaches are viable in Traf code. First, the full annulus model adopts standard periodic boundary conditions with sliding interface planes. A periodic sector of the machine is solved, thus taking into account the actual spatial and temporal domain without any simplifying assumption.

Second, the adoption of phase-lagged boundary conditions assuming chorochronic periodicity, analogous to those described for aeroelastic computations. Chorochronic periodicity of the flow field, allows to significantly reduces the computational costs. All the unsteady computations reported hereafter were carried out by considering a switching RMS residual value 10 times lower than the single precision machine zero, resulting in about 5-10 sub-iterations per time step.

The time step number per period is are chosen so as to well resolve the first two harmonics of the unsteady pressure, keeping a trade off between accuracy and computational costs.

As far as the time-averaged performance computation is concerned, efficiency as well as loss coefficients were defined considering the time averages of mass-weighted total enthalpy and entropy, and work-averaged total pressure.

---

[1]as the ones around blades trailing edges or in blades-endwalls clearences

# 4

# Modal analysis

*In the first part of this chapter a brief dissertation about the modal analyses in cyclic symmetry is presented and the travelling wave spinning modeshapes described together with the FEM setup for modal analyses and the used Open Source tools. In the final part the obtained modeshapes, and in particular its frequency are presented and critically discussed, in comparison with analogous results obtained with a spread used commercial suite.*

## 4.1 Cyclic symmetry model

Painstakingly speaking, a well representative structural and modal analysis must be carried out on a whole domain, but this approach brings necessary to a growth in DOF of the model due to the large number of element of the computational mesh.

This approach is unnecessarily expensive in term of time and computational effort as looking at a typical turbomachinery rows where a single blade or a cluster of blades repeats itself in circumferential direction and "cyclic symmetry" conditions can be applied.

This boundary condition allows the limitation of the structural and modal analysis domain to only one sector without loss of information about the tensile stresses, frequency and mode-shapes of the rows. Obviously even if the single blade domain is formally identical considering an isolated blade or a blade in cyclic symmetry model the resulting mode-shapes can be quite different especially if a strong mechanical coupling between blades is provided.
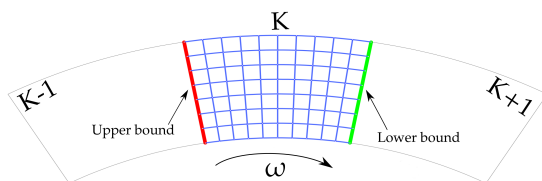


**Figure 4.1:** CSD boundary in cyclic symmetry

As the CDS domain is represented by only one sector of periodicity, a cyclic symmetry set of BC's must be used on the circumferential boundaries to take into account of the neighborhood blocks ($K - 1$ and $K + 1$ in Fig. 4.1). The set of the generalized coordinates and forces for block $K$ can be expressed in a partitioned form

$$\underline{u}_K = \begin{pmatrix} u_K^U \\ u_K^I \\ u_K^L \end{pmatrix} \qquad \underline{F}_K = \begin{pmatrix} F_K^U \\ F_K^I \\ F_K^L \end{pmatrix} \qquad (4.1)$$

- $u_K^U, F_K^U$ the Upper coordinates and forces shared with $K - 1$

- $u_K^I, F_K^I$ the Internal coordinates and forces for $K$

- $u_K^L, F_K^L$ the Lower coordinates and forces shared with $K + 1$

For $K$ sector, if the internal damping is low, the modal analysis results in a classical eigenvalue problem of dynamic equa-

tion of un-dumped system.

$$[M_K]\ddot{\underline{u}}_K + [K_K]\underline{u}_K = \underline{F}_K \tag{4.2}$$

To make the sector analysis consistent, cohesion constraints must be considered

$$\underline{u}_K^L = \underline{u}_{K+1}^U \qquad \underline{F}_K^L = -\underline{F}_{K+1}^U \tag{4.3}$$

The resulting mode-shapes of a general structure which exhibits a axial symmetry is a superimposition of deforming standing wave when the whole model in physical coordinates is considered. The adoption of one sector in cyclic symmetry model move the basis of the modal coordinates from the physical ones to the complex one, and the resulting mode-shapes of the rows as superimposition of deforming spinning wave in circumferential direction (see [57]). Every travelling wave differ from the others from its wave length, or, from a different point of view, for the number of diameter that connect the point of zero-deformation called *nodes* (and so these diameters are called *nodal diameters*) as report in Fig. 4.2.
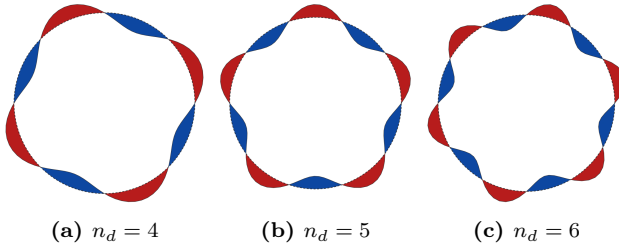


(a) $n_d = 4$      (b) $n_d = 5$      (c) $n_d = 6$

**Figure 4.2:** Circumferential mode-shape with different nodal diameter

So, as the inertial, dissipative, and elastic features are inherently equal for all blades of the rows, the mode-shape is the same for all blades, but shifted in phase of a quantity called IBPA (see eq. 4.5 or eq. 4.5), directly connected with the nodal diameter $n_d$ of the travelling wave.

For even number of blades:

$$IBPA = \frac{2\pi}{N}n_d, \quad n_b \in \mathbb{Z} : -\frac{N}{2} \leq n_d \leq \frac{N}{2} \qquad (4.4)$$

For odd number of blades:

$$IBPA = \frac{2\pi}{N-1}n_d, \quad n_b \in \mathbb{Z} : -\frac{N-1}{2} \leq n_d \leq \frac{N-1}{2} \qquad (4.5)$$

For a given $n_d$, $\pm IBPA$ manifests, and the two travelling waves propagates circumferentially, one in forward direction ($K$ increasing) and the other in backward direction ($K$ decreasing).

In the particular case of negligible mechanical coupling between blades, Upper and Lower set of generalized coordinates are null and $M_K$ and $K_K$ are real and independent from $n_d$, only one eigenvalue is found and so, all eigenvector collapse on a single real mode-shape where all nodes are moving in phase or anti-phase. For the general case where the coupling between adjacent sector is relevant, $M_K$ and $K_K$ are complex and dependent from $N_d$; several eigenvalue/eigenvector are found and the resulting mode-shapes are complex.

## 4.2   Modal analysis results

### 4.2.1   Pre-processing and setup

One of the objective of the work is to test the capability of open source solver and meshing tools to reproduce the modal results obtained by the widespread used Ansys APDL commercial suite. For the FE solver the choice was "CalculiX", an open source tool for analysis and simulation of finite elements, created and developed by an MTU team, with the aim of competing with the other finest finite element suites. The use of Calcuilx is particularly well suited if OMP parallelism on CPU is used, in order to reduce the computational time. Following the same industrial design practice, a similar analysis is carried out and thanks to the industrial partner who provided the results of its internal modal analysis in term of

frequency and displacements of mode-shapes, a comparison between the results can be performed.

As meshing tools the open source platform "SALOME" has been used, as a GUI is present and its output file is directly importable to the CalculiX code. The blade is made of AISI steel and its geometry is not too complex as the airfoil is prismatic and designed with a classical "T-root" suitable for being mounted in a drum configuration. Anyway to fit the small features like leading/trailing edges, fillet, etc.. an unstructured mesh with C3D10[1] elements was revealed as the best choice in terms of flexibility in element size. The blades operate in moderate thermal stress, so to take into account the temperature softening and dilatation effects a constant environment temperature is considered and imposed equal to the average across the row.

Even though interpolation strategies are implemented in CalculiX, for the surfaces in cyclic symmetry, the same superficial discretization is preferable in order to obtain a node-by-node imposition of boundary conditions. The final mesh obtained in SALOME is reported in Fig. 4.3a; to be mesh independent a sensitivity was carried out until the frequency of mode-shape found was uninfluenced by the mesh size.

The blade is mounted in a row on a high spinning rotor, so the centrifugal effect must be take into account both for geometry deformation and for the centrifugal stiffening. To consider all these effects a pre-stress static analysis is carried out and used as input for modal analysis.

The circumferential periodicity of the blade within the rows has been exploited, imposing the cyclic symmetry on tangential boundaries as show in Fig. 4.3b.

### 4.2.2 Modal Results

As the mode-shape is the major input for the flutter analysis, it is important that the two different codes, running with

---

[1]10-node quadratic tetrahedral element

Cyclic symmetry lower bound
Cyclic symmetry upper bound
Contact surface
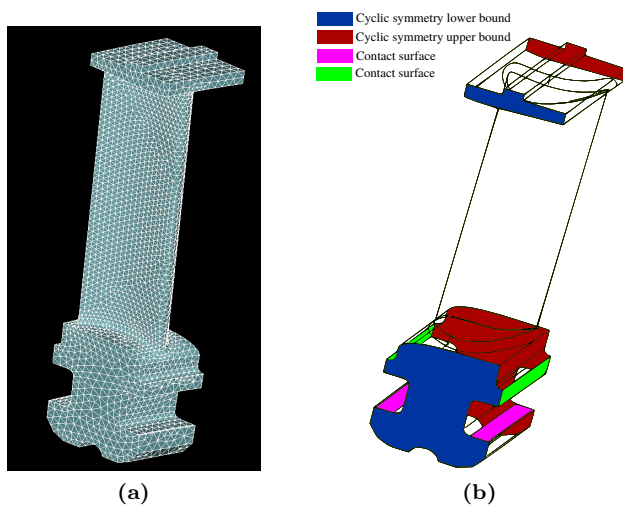Contact surface

**(a)** **(b)**

**Figure 4.3:** CSD mesh and BC's surfaces

the same BC's but with different mesh bring to comparable results in term of mode-shape and frequency.

The first comparison is in term of mode frequency as the damping behaviour of a vibrating blade in a fluid is directly linked to the frequency of the mode-shape. Aeroelastic analysis are commonly performed in order to evaluate the stability of the rows, and, usually the blades who are more susceptible of flutter instability are fan and low pressure rows of turbine and compressor where the blades are slender and usually exhibit the proper frequency around thousand of Herz. But this is not the case of this analysis, where is well know that no flutter occurrence are expected, but rather, the aeroelastic effects are investigated to obtain additional damping.

In this light is not surprising that the blade under investigation, due to its high stiffness and low mass shows proper frequencies decisively higher than the classical values for flutter analyses as show in Fig. 4.4.
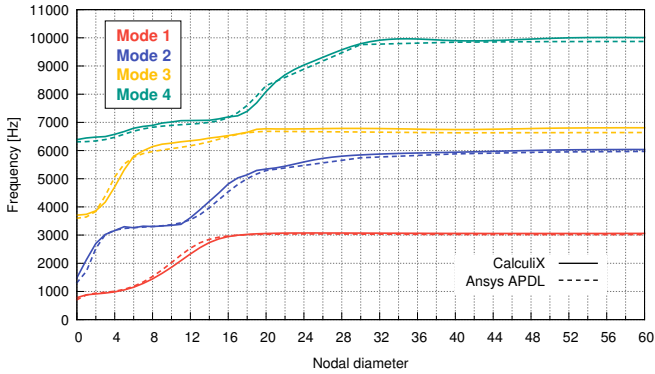
**Figure 4.4:** Ansys Vs. ccx mode-shapes frequencies

The two codes exhibit a good compliance on the results as it is possible to highlight similar trend of the curves for each mode-shape family.In particular for low frequency, an excellent agreement is found, while as the frequency increase the wider differences are recorded.

The obtained mode-shapes are generally complex since the coupling between blades is strong, as confirmed by the fact that for the same mode-shape family a wide range of frequency variation is found from lower to higher nodal diameters.

Referring again to Fig. 4.4 it is possible to see the arise of *mode veering* for low nodal diameters (between $n_d = 7$ and $n_d = 18$), a phenomenon which occurs when two natural frequencies of two different mode-shape families approach each other.

Mode veering draw its name from the behaviour of the trajectories of eigenvalues loci. In fact may happen that two trajectories whose trends would have produced an intersection, when they approached, abruptly veer and following new trajectories instead of crossing.

Using the self-explanatory graph in Fig. 4.5, it can be seen how after veering each locus continues on the path previously

followed by the other. This sharp transition in eigenvalues is accompanied by rapid variations in the eigenvectors, so, for the same mode-shape family, for closer nodal diameters mode-shapes may be very different.
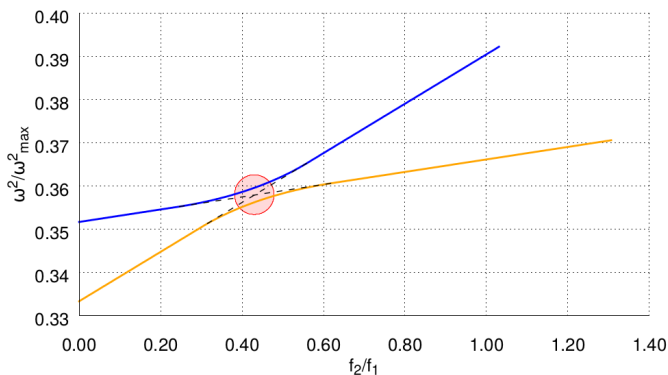


**Figure 4.5:** Modeshape veering

The variation on mode-shape during the veering is difficult to interpret because the modes effectively swap with each other; each one taking on the characteristics of the other and so characteristic of both two family may be simultaneously present on a single mode-shape. This weird behaviour may be the result of approximation in the representation of physical reality as state by Leissa in [58] where offer a elegant and figurative description of mode veering:

> "*A dragonfly one instant, a butterfly the next, and something indescribable in between*".

Taking care not consider a mode-shape closer to veering, just to avoid the issues linked to the complexity of the phenomenon, a visual comparison between the shape of the modes can be perform, to ensure that the simulation are properly carried out by the two different codes.

# 5

# Stage layout and steady computations

*In the first part of this chapter a brief description of the stage layout with its features is performed. Then the different meshes are presented for both multi- and single-rows analyses of the aeromechanical characterization. At the end, the mean aerodynamic results are shown, with several comparisons between the progressive semplification of the CFD setup in order to higlight the best strategy for the following unsteady analyses.*

## 5.1   Stage layout

To properly reproduce all mutual effects between adjacent rows, a 1.5 stage domain is considered as shown in Fig. 5.1 where the real meridional flowpath is reported.

The 1.5 stage exhibits the common features of HP stages; the rows are designed with high aspect-ratio an low radius-ratio to work with a reaction degree of about 50%. The blades are mounted in a drum configuration with high blade count (more than one hundred for each row) on a quasi-cylindrical
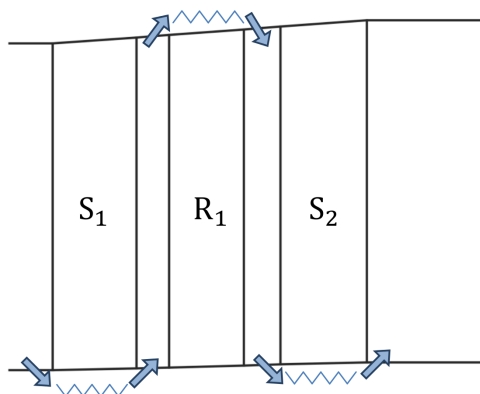
**Figure 5.1:** Meridional flowpath and shroud leakages position

flowpath and in order to avoid tip leakages losses, the blades are equipped with a tip shroud, whose position is schematically shown in Fig. 5.1.

To account for it, a simple one-dimensional model of shroud cavity was included (see [59], [60]) in the computations. Briefly, for a specific shroud geometry, the model calculates the leakage mass flow, total enthalpy rise and change in angular momentum through the cavity and the flow conditions at the interface between the cavity and the mainstream. Following an approach similar to the one proposed by McGreeham and Ko (see[61]), the flow through the shroud cavity is completely modeled, and its interaction with the main flow path is calculated by imposing coupled source/sink boundary conditions at the cavity/mainstream interface.

## 5.2   Steady computations

### 5.2.1   Mesh

For the discretization of the computational domain, a 3D structured viscous H-grid of about 0.9M elements was used

for each of the three rows. In the Fig. 5.2 is report a blade-to-blade computational mesh which lies on surface at midspan. Indeed "classical flutter analysis" are commonly performed with isolated row an so, being the rotor blade the subject of interest of the characterization only the rotor grid will be used for flutter calculations. In the last part of the thesis (Chapter 8) some unconventional flutter computations will be carried out using the multirow grids with vibrating rotor to take into account some coupling effects between the unsteadiness of rows interaction and the ones coming from rotor vibration
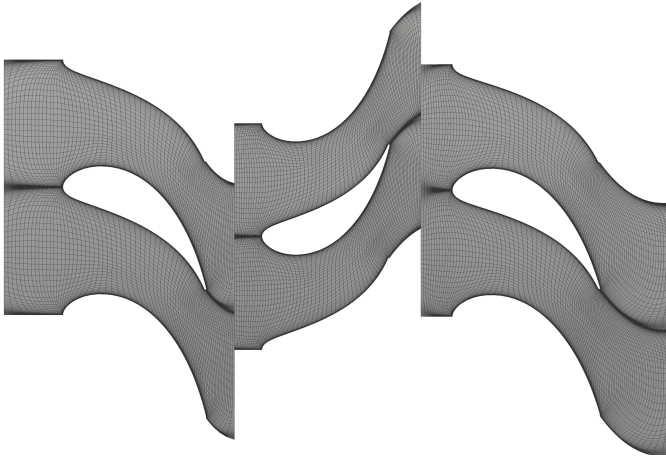


**Figure 5.2:** Blade do blade grid @50%span

The generated grids will be used in all computations using full Navier-Stokes calculations, but to reduce computational effort, especially in computing times, as suggested by Pinelli et al. (see [30]) the effect of the boundary layer on the endwalls can be neglected, solving only boundary layers on the blade surfaces without losing accuracy in the prediction of aerodynamic damping.

This type of calculation herein called "inviscid endwalls" allows to drastically reduce the number of mesh elements, with a consequent decrease in the calculation times.

In Fig. 5.3 the two types of mesh are reported to high-
light the different spanwise cells distributions[1] and the lack
of spanwise boundary layer on the endwalls of the inviscid
mesh.
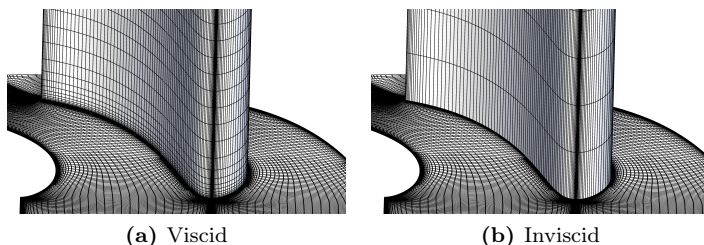


**(a)** Viscid         **(b)** Inviscid

**Figure 5.3:** Full-NS vs. Inviscid mesh

To confirm the applicability of this approach, the blade
loading coming from the full-NS simulations and the ones
from inviscid endwalls are compared. Note that that the sim-
ilar shapes in load profiles with the same blade vibration lead
to the same aerodynamic work (and thus the same logarith-
mic decreasing value is found).

## 5.2.2 Steady results

The steady analysis represents the first step of flutter com-
putations which need an initialization flow. Therefore the
steady set-up must be carefully chosen. As BC's imposed on
inlet/outlet of the 1.5 stage domain, a set of spanwise dis-
tributions representative of an operative design point near
the maximum of efficiency is chosen and mixing planes at
rows interface are used. The 1.5 stage solution in useful
both for initializing multirows unsteady computation, and
both to extract the boundary conditions on rotor row (where
the aeromechanical characterization is focused on). The ex-
tracted inlet/outlet BC's for the rotor are subsequently ap-

---

[1]Here is reported the only the rotor blade

plied to an isolated row simulation and used for classical flutter computations.

The working condition where the aeromechanical characterization of the blade is request, is the design point, where commonly operates; In this conditions, this kind of stages usually does not show odd structures of flow field (like shock waves or separation bubbles).

Focusing on the rotor blade, as shown in Fig. 5.4a, the isentropic Mach number flow field of the blade-to-blade midspan surface shown a typical subsonic flow field of high pressure stage and in particular as the incidence pointed out by the streamlines in Fig. 5.4b is the one expected from the design point.



(a) Mach number          (b) Streamlines
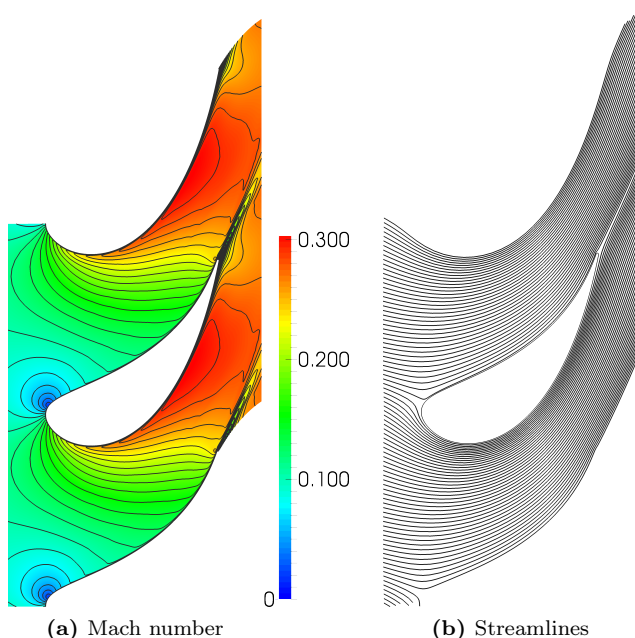
**Figure 5.4:** Flow field @50%span

All the simulations were performed with the HRN $k - \omega$ turbulence model (refer to appendix A for turbulence model

detail) and as the blade have a tip-shroud, the simulation was carried out by activating the model that simulates the shroud leakage. The use of this model could often worsens the convergence of the calculation, as in addition to the main flow the shroud leakage must also be modeled with extraction and re-injection of a mass flow rate across the blade (see Fig. 5.1).

Keeping in mind that for the aeromechanical characterization purpose, starting from similar blade loading, similar aerodynamic work are expected, a simplified solution without take into account the shroud model is tested. As the shroud leakages are modelled rather than simulated, for this reason the mesh was not modified, and the shroud model was simply switch off to obtain an unshrouded solution.

The comparison reported in Fig. 5.5, shows a typical aft-loaded distribution of isentropic Mach number, with an exit value of about 0.3 with almost the same trends for both shrouded and unshrouded simulations. The influence of the shroud model on blade loading is tangible only for a small percentage on the span in near tip region, while for the other part of the blade the effect is practically negligible.

Once the relevance of the shroud model was assessed, further to speed-up the calculation, a setup with the inviscid endwalls model is tested (see section 5.2.1). Obviously the adoption of the inviscid endwalls model rather then a fully N-S computations must be legitimated for the unsteady runs, despite the fact that the quasi-cylindricity of the meridional flowpath, the lack of odd structure of motion in flow, in addition with high-aspect blades are factor that push in the right direction towards to the validity of the inviscid layers approach. Using the blade loading coming from full Navier-stokes CFD setup as goal to follow, another comparison is fulfil with the inviscid endwalls.

As shown in Fig. 5.6 the impact of endwalls boundary layer on blade loading is practically negligible and so no difference are expected in aerodynamic work evaluation if one or the other solution is used as initialization for aeroelastic computations. As the subject of this work is to outline a strategy appealing for industry where the computational time are im-

portant in a design phase, the time reduction given by the inviscid endwalls computation due to the slender meshes is appealing.
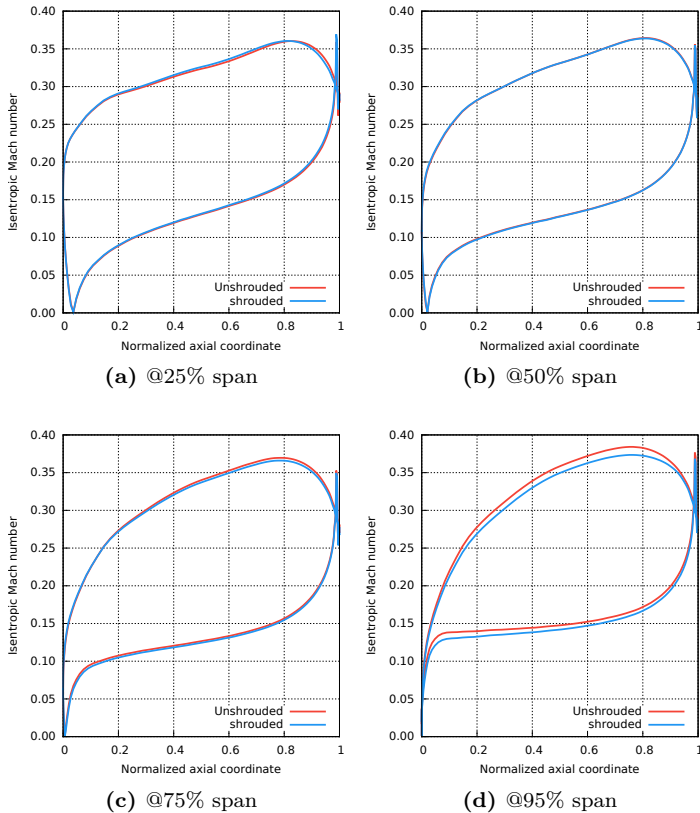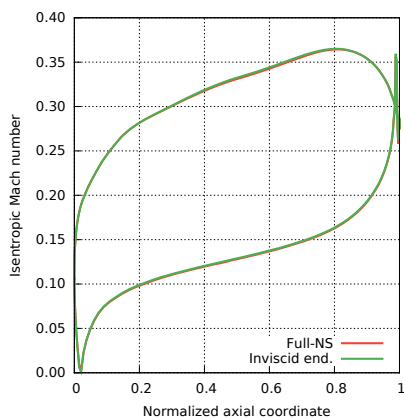


**(a)** @25% span

**(b)** @50% span

**(c)** @75% span

**(d)** @95% span

**Figure 5.5:** Shrouded/unshrouded steady state comparison

Anyway, even if the validity of the approach is already proved (see [30]) to have a deep insight in the results and to certify the validity of the approach with inviscid endwalls

both steady solutions[2] are used as initialization for the un-
steady computations.

In this way, two logarithmic decrement curves curves are
obtained, so possible differences in the results might be high-
lighted and in the other hand the approach can be consider
valid.



**(a)** @50% span
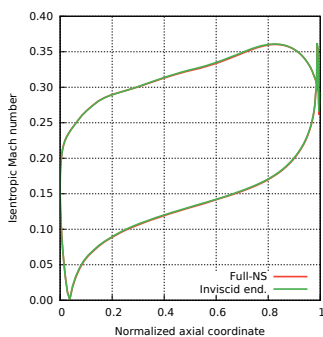


**(b)** @25% span
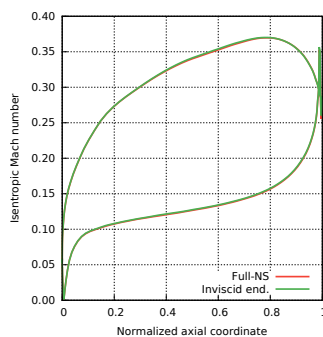


**(c)** @75% span

**Figure 5.6:** Full-NS vs. Inviscid endwalls blade loading

---

[2]The other is the unshrouded full Navier-Stokes

# 6

# Classical flutter computations

*In this chapter, the results of modeshapes transfer from structural to fluid dynamic grid will be show. Later, the aeromechanical strategy adopted for single blade flutter computation will be presented and the obtained results discussed. In the final part of the chapter the focus of the activity move on the study of the effect of modeshape veering on logarithmic decrement curves.*

## 6.1 Modeshape transfer results

Since to the numerical method for aeroelastic computation is uncoupled, the early steps of unsteady simulations are dedicated to reproducing on CFD grid blade surface the modeshapes coming from the previous modal analysis. As the flutter computations takes into account only the vibrating aerodynamic surfaces, from modal analysis only the displacements relative to airfoils must be extracted and "cloned" on CFD mesh as described in chapter 3.2.1.

The modeshape transfer results for a complex modeshape of an intermediate $n_d$ of the $2^{st}$ modeshape family is reported[1] in Fig. 6.1.



**(a)** CSD modeshape $\mathbb{R}e$



**(b)** CFD modeshape $\mathbb{R}e$



**(c)** CSD modeshape $\mathbb{I}mm$
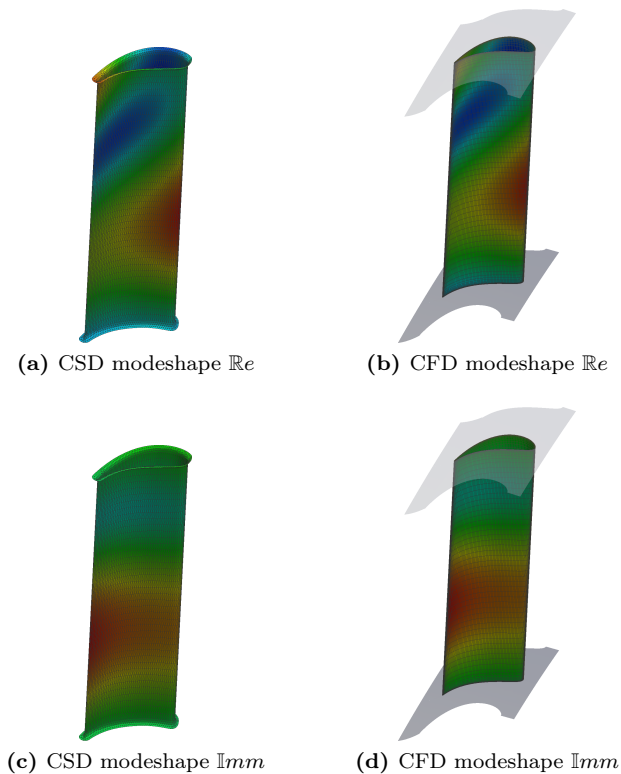


**(d)** CFD modeshape $\mathbb{I}mm$

**Figure 6.1:** CSD to CFD modeshape transfer

As can be seen, the CDS modeshapes is well reproduced on the CFD grid with a very satisfying agreement. Simultaneously to modeshape transfer, the deforming grid is obtained

---

[1]Due to the large number of nodal diameters, for a sake of conciseness all results of modeshape transfer are not included

splitting the vibration period in a discrete number of temporal steps.

No re-meshing or morphing techniques are need to build it, and the grid is deformed with deformations phasors with sinusoidal functions. In Fig. 6.2 the blade deformation at midspan over a vibration period is superimposed to the undeformed geometry; to highlight the deformation a well emphasised vibration amplitude is adopted.



Undeformed

Deforming geometry
according with modeshape
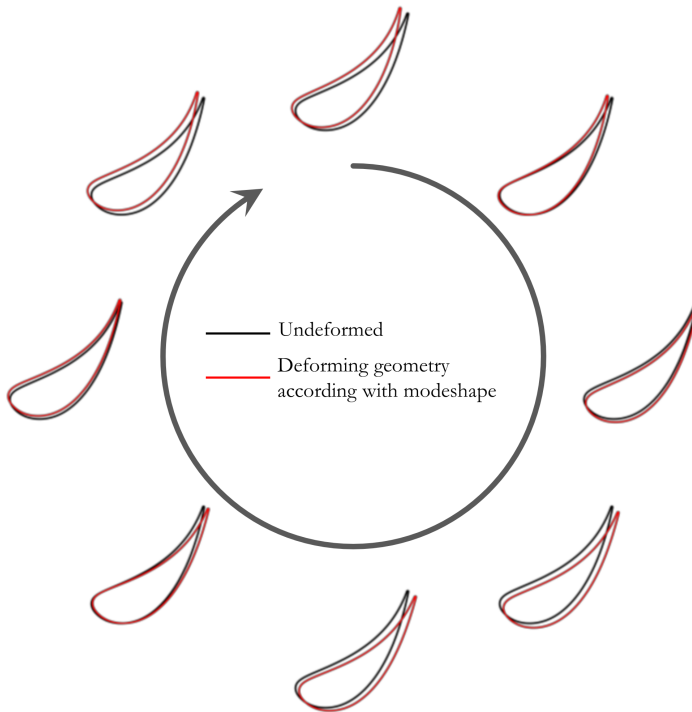
**Figure 6.2:** Geometry deformation over vibration period
(magnified)

# 6.2 Aeroelastic computations strategies

One of the first issue to be faced before starting with flutter computations is to pinpoint the best setup of unsteady runs to get the best compromise in term of accuracy and computational time effort. To follow this purpose, as the computational time is straight linked to the size of the mesh discretization, a bibliographic research activity in the early stages of works was carried out to identify the more common size of the grid for this kind of simulation. Another crucial step for the accuracy of unsteady computation results is the choice of the time-step sampling of the vibration period; from one hand a under-sampled period does not allow to correctly resolve the $1^{st}$ harmonic pressure, an then a wrong value of aerodynamic work is computed, to other hand, a over-sampled period makes the unsteady run more time demanding to resolve higher order harmonic of pressure which does not affect the aerodynamic work.

As aerodynamic work is basically evaluated from the first harmonic of non-stationary pressure, a periodic solution is required to properly evaluate aerodynamic work. Although there are no rows interactions, as classical flutter computations consider an isolated row, the only source of unsteadiness is present due to the vibration of the blade. As standard for flutter computations, dividing the vibration period in 80 equally spaced time steps is the best setup for low to high frequency modeshapes, usually analyzed for aeroelastic computations.

Once the flow field has been initialized from the steady solution, the unsteady simulation has been carried out with a dual-time marching technique for each of all sampling timestep during the period, solving in the pseudo-time up to a predetermined residue before moving to the next physical time step until the periodicity is reached. To analyze the goodness of periodicity achieved, the evolution of a lift coefficient based on the blade surface pressure together with the trend of the

logarithmic decrement after each period are monitored during the solution as report in Fig.6.3 where the convergence outputs for a travelling wave with IBPA=180° is show.

A 2-blocks CFD computational domain with phase lagged boundary conditions is adopted and so it is possible to evaluate the blade loading on the airfoils surfaces of both of them. Noteworthy as further confirm of a well-reproduced modeshape, due to for IBPA=180° the blade moves in anti-phase, the blade loading are in antiphase too (the two blocks see the same blade loading but shifted by an IBPA due to travelling wave deformation)
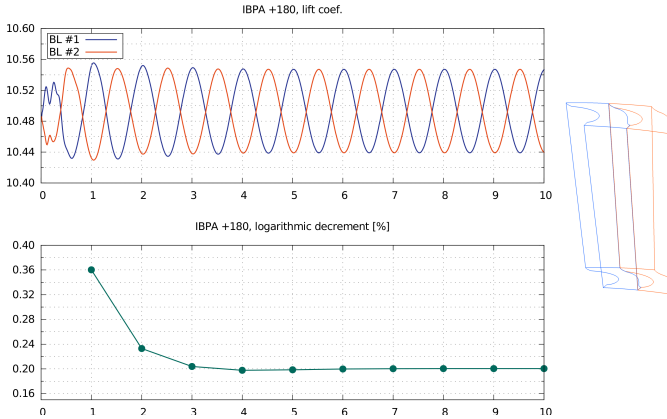


**Figure 6.3:** Typical convergence history

One of the main purposes of the aeromechanical characterization is to obtain a value of critical damping ratio suitable to be used in term of logarithmic decrement (according to eq. 2.2) in the dynamic analyses as an additional dampers due to fluid flow with those mechanics.

$$\Delta_{TOT} = \delta_M + \delta_F \tag{6.1}$$

To compute the logarithmic decrement (eq. 2.3), the integral value of aerodynamic work $\mathcal{L}$ is considered and so $\delta_F$ is a parameter which characterize the global damping behaviour

of the analyzed blade connected to the flow, but in some cases such as redesign due to flutter issues, it is also useful to know the surface density of this value to highlight the zones of the blade where the main work exchanges occurs. To have a deep insight on this aspect, a density of energetic damping can be defined as follow:

$$\rho_\xi = \frac{-dL_\delta}{8\pi E \frac{dS}{S}} \tag{6.2}$$

where:

- $dL_\delta$ is the local work on grid cell

- $dS$ is the surface of CFD grid cell

- $S$ is the whole blade surface

- $E$ is the blade average kinetic energy

This parameter, can be plotted over the blade surface, highlighting the areas of the blade that have more influence on global aerodynamic damping as shown in Fig. 6.4.

Integrating the local quantity defined in 6.2 over the whole blade surface, the numerator yields to the aerodynamic work as sum of local works, while the $dS/S$ in the denominator becomes the units. In other words, integrating $\rho_\xi$ over the blade surface the critical damping ratio defined in 2.2 can be re-obtained in an alternative way.

## 6.2.1   Endwalls boundary layer effects

To speed-up the unsteady calculations, a reduction in mesh density undoubtedly goes in the right direction, therefore, a first attempt can be perform neglecting the boundary layer on endwalls in spanwise direction. This approach allows to re/duce considerably the mesh node count, and in particular for the ones used for flutter computations, from 80 cells in span wise direction to 16. As already verified in chapter 5.2.2, this severe reduction affect the blade loading
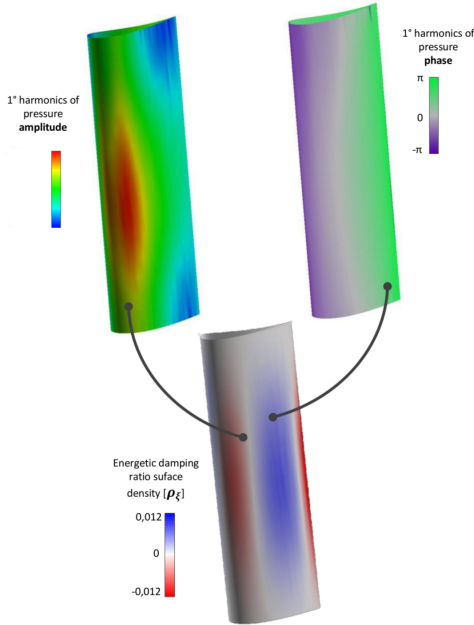
**Figure 6.4:** Blade distributions of aeroelastic quantities

in a negligible way, and so for the purpose of aeromechanical characterization no relevant difference are expected.

To quantify the time saving obtained using the inviscid endwalls formulation, a comparison with a viscid endwalls run is carried out. As representative of a common complex modeshape, the $n_d = 14$ of the $1^{st}$ modeshape family with the $IBPA = 42°$ travelling wave is chosen.

To get a consistent comparison between the results, the two runs are achieved using the same setup in term of temporal discretization, convergence goals and number of period computed. The computation have been performed on the same number of CPUs[2] with same architecture an levels of

---

[2]Intel(R) Xeon(R) CPU X5650 @ 2.67GHz

|  | Viscid endwalls | Inviscid endwalls |
|---|---|---|
| $np_x$,$np_y$,$np_z$ | 144x72x80=∼0.83M | 144x72x16=∼0.17M |
| Comp. time [s] | 2.91E+04 | 5.7E+03 |

**Table 6.1:** Viscid/Inviscid unsteady runs performances

OMP parallelism and the obtained results in term of computational time have concisely been collected in table 6.1.

The method was already validated by Pinelli et al. in [30], anyway to confirm its goodness a comparison between viscid/inviscid endwalls, aeroelastic results are carried out by overlapping the logarithmic decrement curves obtained all over IBPAs. The full Navier-Stokes with viscid endwalls has been considered as benchmark as the more accurate setup for accurately compute aeroelastic evaluations, even if more demanding in time and computational effort. For the sake of clarity, the logarithmic decrement curves for the $1^{st}$ mode are reported below in Fig. 6.5, but will be adequately discussed in the dedicated sections 6.2.2.
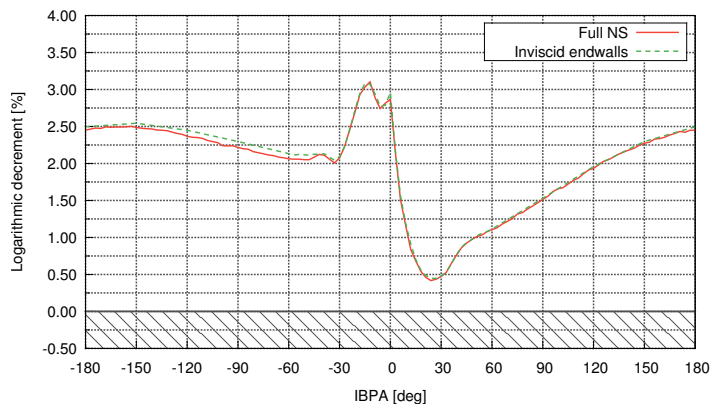


**Figure 6.5:** Viscid vs. Inviscid endwalls comparison for mode 1

As can be seen, the inviscid endwalls simulations are fully capable to reproduce the results obtained from the ones coming from the viscid endwalls simulations in a very satisfactory manner for all computed IBPAs. The slight over-estimation for negative IBPAs is considered fully acceptable as a good compromise with respect to the amount of time saved shown in table 6.1.

As results of these comparison, the CFD setup with inviscid endwalls simulations has been considered as the standard for all single blade classical flutter computations, in the light of all the benefits in term of accuracy/time saving with respect to viscid endwall setup.

### 6.2.2   Mode 1:

Starting with the first family of modeshapes, the flutter analyses are carried out in order to obtain the logarithmic decrement curves all over computed IBPAs.
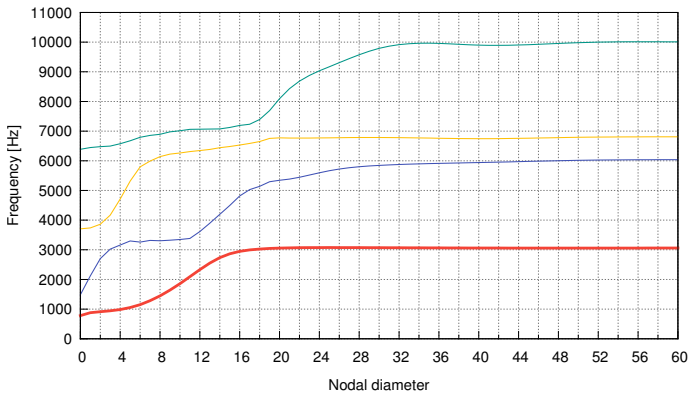


**Figure 6.6:** Mode 1 (red) frequencies

Referring to the graph of the frequencies trend shown previously in Fig. 4.4 and shown in Fig. 6.6 for completeness by highlighting the mode 1, it is possible to see how the frequency has a steep ramp for lower nodal diameters starting

from about 760 Hz for $n_d = 0$ up to 2680 Hz for $n_d = 16$. Due to this wide variations is strictly connected with the variations of eigenvalues, and a wide variation in modeshape is expected, with a resulting effect on the shape of logarithmic decrement curves. In Fig. 6.7 the logarithmic decrement curve is report over all computed IBPAs of the mode 1. The analyzed mode shows an always positive logarithmic decrement as desired. Therefore the aeroelastic interaction between the vibrating blade rows and the fluid plays a positive role, and it can be exploited as an additional damping effect.

Looking at the frequency curves in Fig. 6.6 it is reasonable to suppose that when the frequency value does not abruptly change for closer nodal diameters ($nd > 16$) the relative modeshapes are quite similar. For this reason the computed traveling waves must be clustered around $n_d = 0$ to assure to capture all effects of $low - n_d$ frequency variation. When the frequency remain almost constant some IBPAs can be skipped in order to reduce the global time request, without loss in prediction in the shape of the curves.
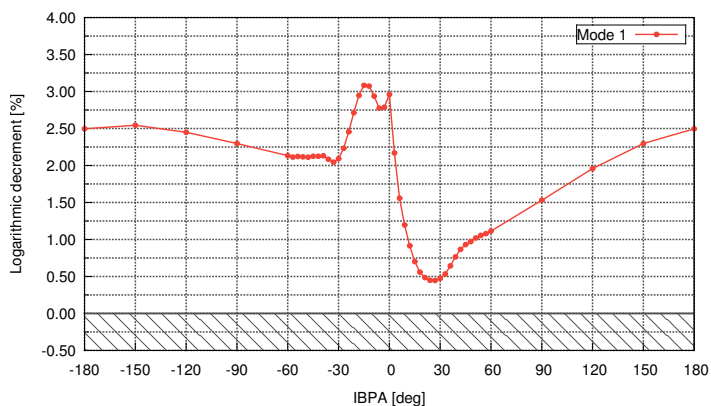


**Figure 6.7:** Mode 1: Logarithmic decrement curve

Looking again at Fig. 6.7, an "odd" trend for IBPAs closer to 0 stand out, so, to well understand this behaviour, the

amplitude and phase of the $1^{st}$ harmonic pressure was investigated.

In Fig. 6.8 the $1^{st}$ harmonic of pressure have been reported in term of amplitude and phase for the two travelling waves with IBPA=±150 (closer to the left/right extremities of the curve of logarithmic decrement) ad for the standing wave IBPA=0°.
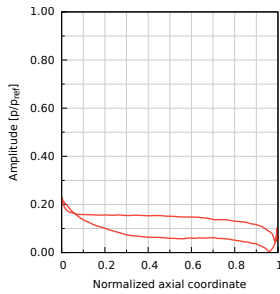
Referring to Fig. 6.8a, 6.8c and 6.8e is immediate to deduce how the amplitude of the pressure harmonic for IBPA=0 is considerably lower than those for higher IBPAs, meaning that the interaction between vibration of the blade and fluid flow, in this zone of the curve is significantly less intense.
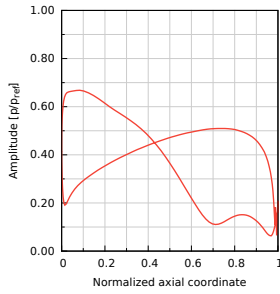
**(a)** IBPA -150, amplitude
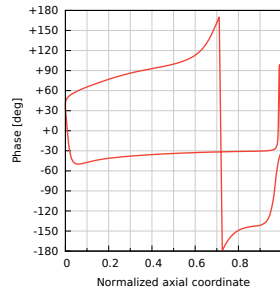
**(b)** IBPA -150, phase
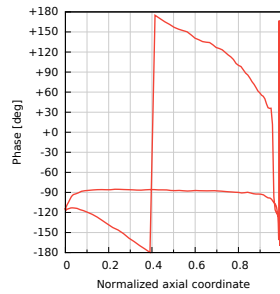
**(c)** IBPA 0, amplitude

**(d)** IBPA 0, phase
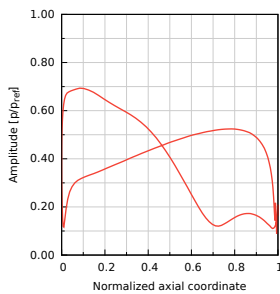
**(e)** IBPA +150, amplitude
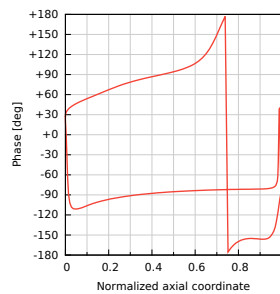
**(f)** IBPA +150, phase

**Figure 6.8:** Mode 1, $1^{st}$ harmonic of pressure

In order to obtain a complete overview of this aspect, the amplitude of the first harmonic of pressure for all IBPAs is reported with a colormap in Fig. 6.10a related to all over IBPAs and normalized arcwise coordinates defined as in Fig. 6.9.

A similar map is obtained for the phase the first harmonic of pressure and report in Fig. 6.10b.

Considering both the frequencies of the modes reported in Fig. 6.6 and the just mentioned maps in Fig. 6.10 at the same time, it can be noticed that in the zones where the frequency increases quickly (for low nodal diameters up to $n_d = 16$) the amplitude of the first pressure harmonic has a generally a lower value (represented by the blue belt for the IBPA around zero in map Fig. 6.10a). At the same time, from the phase map, in the same zone a very high variability is observed, even with high jumps in phase value.
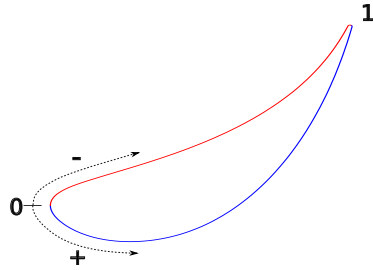


**Figure 6.9:** Normalized arcwise coordinate

The higher variation of the phase means that vibration modes associated to closer nodal diameters are substantially different each other and also that the pressure response is lower. On the other hand a phase that varies with continuity for closer node diameters, as it is found for travelling waves with high IBPAs, means in a more regular trend of the logarithmic decrement curve ad usually found for common flutter analyses.

Although the shape of the logarithmic decrement curve for the traveling waves near zero finds its justification in the high frequency variability and in the form of vibrational modes, it is still unclear why the value of the IBPA=0° is different from the other values laying on the curves

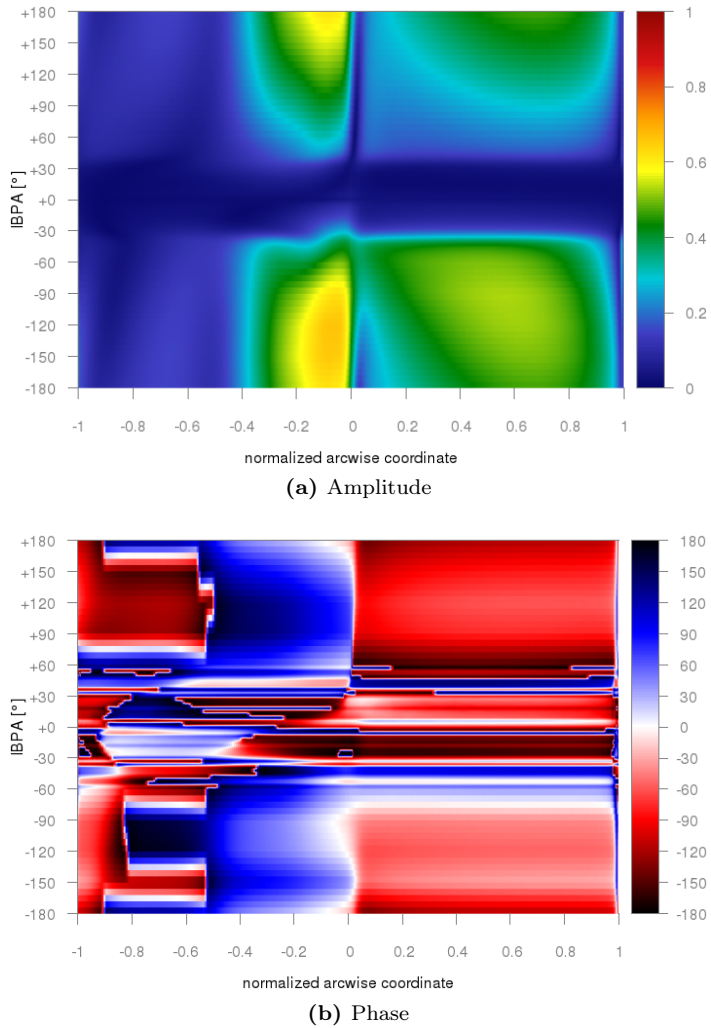**(a)** Amplitude



**(b)** Phase

**Figure 6.10:** Mode 1, $1^{st}$ harmonic of pressure maps

Looking at the definitions of energetic damping coefficient and logarithmic decrement reported respectively in Eq. 2.2

it can be seen how the value of logarithmic decrement it is essentially driven by the ratio between the aerodynamic work and blade average kinetic energy.

The aerodynamic work is the results of the computation, as the main input for aeroelastic assessment, while the kinetic energy can be easily computed starting from the modeshape frequency and modal mass and for this reason these two quantities can be plotted over IBPAs as report in Fig. 6.11 where the normalized value are used.

For those nodal diameters which exhibits a quasi-constant frequency respect to its neighbor ones, the kinetic energy remain stable (in other words IBPAs>48 or IBPAs<-48), whereas, for $n_d$ which bring to $-48 \leq$IBPAs$\leq 48$) the wide frequency variations affect in the same way the trend of kinetic energy.

This is why, the extremes part of the logarithmic decrement curve are regular being the trend essentially driven by the trend of aerodynamic work, due to, being the kinetic energy constant its effect in only a scale of the value of aero-
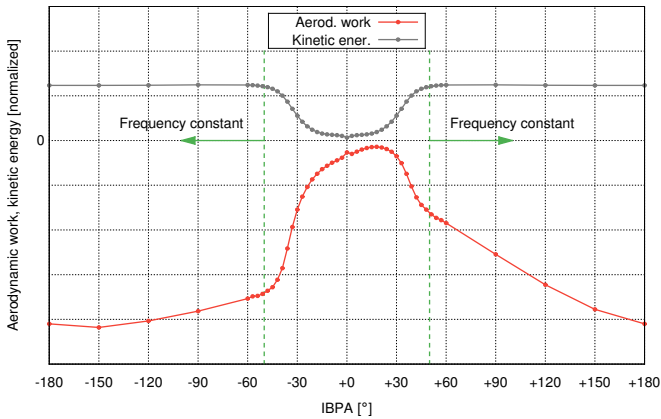


**Figure 6.11:** Mode 1: Aerodynamic work and blade average kinetic energy

dynamic work without affecting its shape. In the core region of logarithmic decrement curves, aerodynamic work and kinetic energy present both its own shapes, thus the resulting logarithmic decrement shape is a combinations of the two tendencies, according to the Eq. 2.2, 2.3.

### 6.2.3  Other modes results

As far as the $2^{nd}$,$3^{rd}$ and $4^{th}$ modes are concerned, the flutter results are obtained in a similar way for the $1^{st}$ mode and the obtained logarithmic decrement curves are reported in the appendixes B, C and D and also reported here on the same plot in Fig. 6.12 for enhance the fluency of the thesis.
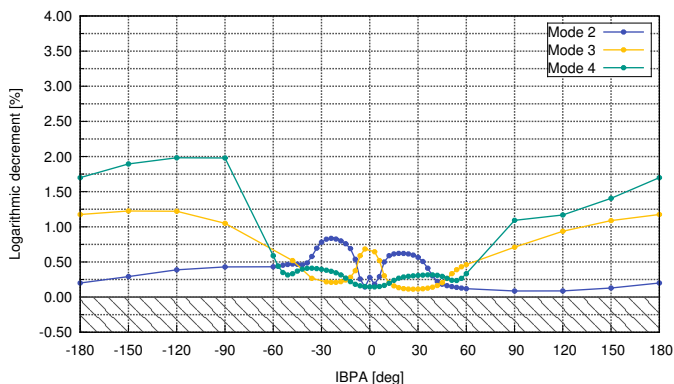


**Figure 6.12:** Other modes: Logarithmic decrement curve

Referring to Fig. 6.12, the same considerations done for the $1^{st}$ modeshape family are still valid. The sharp variation in frequency for low nodal diameters results in a higher variability in the shape of logarithmic decrement curves.

From the curves in Fig. B.2, Fig. C.2 and Fig. D.2 it possible to see how for the inner IBPAs a lower aerodynamic work is found respect to the one exhibit form the outer IBPAs; this effect is to ascribe to a generally lower interaction between the fluid and the blade for IBPAs closer to zero. This aspect

is quantifiable in the overall colormaps for the amplitude and phase of the $1^{st}$ harmonic of pressure reported in appendices in Fig. B.4, Fig. C.4 and Fig. D.4.

From the amplitude map its possible to highlight the "blue belt" for inner IBPAs, representative of the low interaction with fluid, while for outer diameters the amplitude grow an then a higher aerodynamic work is found.

From the phase map it's possible to highlight how in the core region the phase shown abruptly variations as a symptom of a quickly change in the shape of the modes for closer modal diameters.

For all modeshapes analyzed, due the high variability of the modeshapes for this type of blades, the classical effect of the increasing in damping with higher frequency is not an aspect generalizable or extensible to other similar geometries.

With respect to the typical geometry flutter investigated, in which mode frequencies are lower and practically constant, the link between the shape of logarithmic decrement and aerodynamic work is difficult to be captured. Indeed, due to variability of the trends of both aerodynamic work and kinetic energy over IPBAs, the resulting shape of logarithmic decrement can not be generalizable.

## 6.3    Mode veering effects

As already shown in section 4.2.2, from the modal analyses, the arise of mode veering phenomenon between neighbor modeshape family is found for low nodal diameters. Since the veering effect afflict the modeshapes of those nodal diameters involved, is reasonable to suppose that a tangible effect on resulting logarithmic decrement curves can be found, by reason of a modeshape swapping between modeshapes family is produced.

In order to evaluate the effect of mode veering on the logarithmic decrement curves, and to be sheltered by the effect of the large frequency variation, three fictitious curves at

constant frequency are obtained by extracting flutter results from the calculations already carried out.

Three frequency $f_1$, $f_2$ and $f_3$ are chosen for collecting the logarithmic decrement coming from the previous calculations, with a tolerance value referred to the nominal value of frequency in order to collect as many modeshapes as possible.

In Fig. 6.13 the three constant frequency $f_1$, $f_2$ and $f_3$ are displayed; in particular $f_3$ involves some low nodal diameters of the $5^{th}$ modeshape family which is not included in the previous computations due to its high frequency and out of industrial interest.
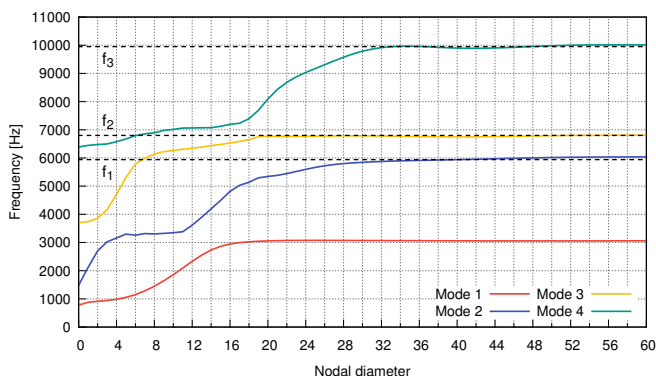


**Figure 6.13:** $f_1$, $f_2$ and $f_3$ for modeshapes collecting

To perform this kind of analysis at constant frequency this few nodal diameters belonging to the $5^{th}$ modeshape family are computed for completeness.

In Fig. 6.14 are reported the results of the selection of the logarithmic decrements coming from the nodal diameters with a quasi-constant frequency but belonging to different mode-shape families, highlighting the family to which the modeshape vibration originally belonged by means of different coloured circle markers.
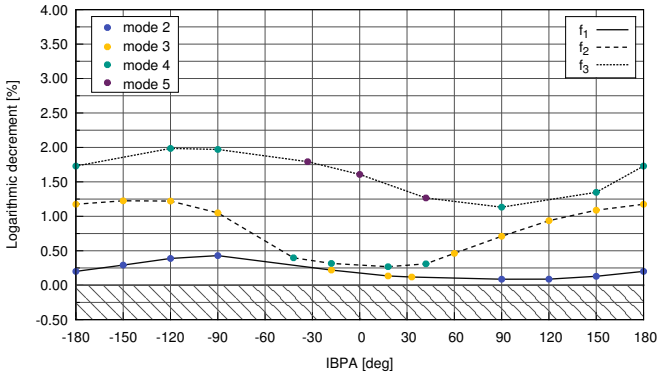
**Figure 6.14:** Logarithmic decrement curve at constant frequency

As can be seen, these curves exhibits a pseudo-sinusoidal trends similar to the ones evidenced in the literature for turbine blades typically subject to flutter.

This results justify the unusual shapes of the logarithmic decrement curves compute in this work. On the one hand this is due to the wide variation of the modeshape family frequency, on the other hand for a different pressure response especially a lower nodal diameters.

All results obtained from the study of blades damping behaviour have been merged in the paper [62] presented at TurboExpo 2016 technical conference.

# 7

# Stages interaction forcing effects

*In this chapter, forcing effect due to stage interaction will be quantified through CFD unstedy computations. To clearly identify the sources of unsteadiness, the spectrum of the resulting force, obtained through a DFT on its signal, is studied and to pinpoint the contents of the fundamental harmonics, an acoustics discussion following Tyler and Sofrin will be carried out.*

Alongside the evaluation of aerodynamic damping, the other fundamental aspect of the aeromechanical characterization of the blade under investigation entails the evaluation of the synchronous forcing effects. Historically, these effects have been firstly studied to provide the imput for the balde dynamic analyses, even before the numerical methods became popular in the industrial design practices. Several correltions or 0D/1D approaches, have been developed over the years, which are nowadays still used in the early design phases, where the degree of uncertainty in forcing evaluation is tolerated thanks to their quick use and readiness of the results.

Currently, the steam turbine technology is long-established, especially for the stages like the one under investigations. For this reason, the more and more pressing demand in increasing performances make the improvement margins very narrow and the blades must be designed, although with the required safety margins, to the limit of their mechanical performances. That's why in the final phases of verifications of the row, it is not tolerable to deal with the uncertainty given by the simplified approaches on the estimation of aerodynamic forcing. This part of the work is devoted to the definitions of the sources and the estimation of magnitude of aerodynamic forces acting on the rotor blades by the means of CFD analysis methods in the branch of aeroelasticity commonly referred as "forced response" as stated in 2.2.1.

The more common and relevant source of synchronous forcing is the rotor/stator interaction, so, even if only the rotor blade is under aeromechanical investigations, both upstream and downstream stators rows must be takes into account in CFD computations using the 1.5 stage layout as fluid domain. The main purpose is to find out the aerodynamic forces on blade with high accuracy, and for this reason, all the simplifications like the inviscid endwalls and the suppression of the shroud model are not used anymore in this part of the activity, where a fully 3D Navier-Stokes computations with viscid endwalls is preferred as more accurate.

## 7.1    Rows interaction: Forcing effects

As the forcing effects on the blade are essentially due the unsteady pressure field on its skin surfaces, a simple steady approach with mixing plane between adjacent rows it's non usable, due to the fact that all incoming unsteadiness would be mixed and their effects on rotor cannot be evaluated; so, it is clear that the all evaluations about forcing effect must be carried out by using unsteady simulations with the following issues. The first one is about the computational time that for unsteady analyses play a relevant role about the usability and

readiness of the results. Moreover due to the fact that high pressure stages commonly exhibit a large number of blades for each rows, if the blade counts came in coprime relation, a very large number of tangential sector must be computed due to the periodicity is achieved on the whole full annulus. If a tangential periodicity over the sectors is found, it can be exploited to reduce computational effort, but in this optic the adoption of a phase lagged formulation for the tangential BC's (see [55]) allow the maximum reduction.

All unsteady computations have been computed by using the 1.5 stage mesh displayed in 5.2, a 3 rows H-Type grid of about 0.83M elements/row suitable to well reproduce the boundary layer with a $y^+ \sim 1$ on the blade computational surfaces.

The main sources of aerodynamic forcing effects on the rotor row, are due to the its interaction with the stators. As upstream interaction the forcing effect is due to the incoming wakes generated by the stator S1 (Fig. 7.1a), while, for downstream interaction the forcing effect on the rotor R is caused by the passage of the potential field of the S2 stator (Fig. 7.1b).

Each of the two forcing effects, acts with a frequency synchronous with respect to the rotor speed therefore the frequencies of both of them is equal to the respective blade passing frequency (BPF)

$$BPF_1 = \frac{n}{60} Z_{S1} \qquad (7.1)$$

$$BPF_2 = \frac{n}{60} Z_{S2} \qquad (7.2)$$

The main effect for aeromechanical characterization due to the rotor-stators interactions is that the pressure on the blade skin surface shows an unsteady behaviour with a periodic oscillation over a blade passage.

To obtain the resulting force $(F^{TOT})$ over a period, its components in tangential $(F_T)$, axial $(F_X)$, and radial direction $(F_R)$ have been computed at every time-step of the simulations as unsteady effect on whole blade surface.
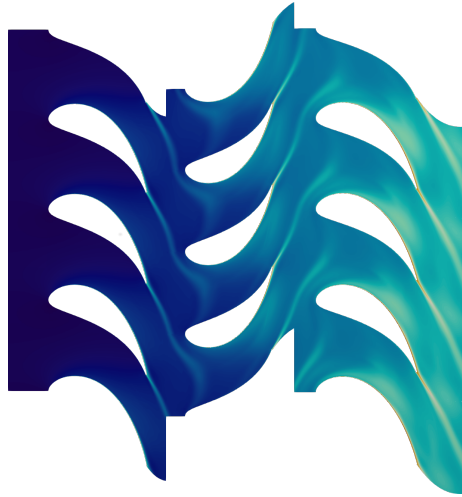
**(a)** Incoming wakes
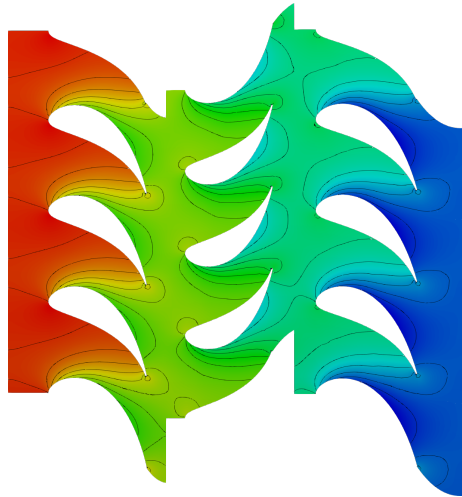


**(b)** Potential field

**Figure 7.1:** Rotor-Stators interactions

The trends of the force components have been reported in Appendix E in Fig. E.1a, Fig. E.1b and Fig. E.1c as percentage of the period of the simulation. As expected, the main contributes to $F^{TOT}$, comes from $F_T$ and $F_X$ which are similar in magnitude, while $F_R$ is quite lower as expected.

Once the three contributes are available for all time-steps, simply combining $F_T$, $F_X$ and $F_R$, $F^{TOT}$ is computes and its trend is reported in Fig. 7.2.

$$F^{TOT} = \sqrt{F_T^2 + F_X^2 + F_R^2} \qquad (7.3)$$

From the composition of $F_T$, $F_X$ and $F_R$, $F^{TOT}$ shows an amplitude modulation by a low frequency, which is a blade passing frequencies combination and so to have a deep insight on the harmonics contents of $F^{TOT}$, a DTF analysis have been performed on the signal obtaining the frequency spectrum shown in Fig. 7.3.
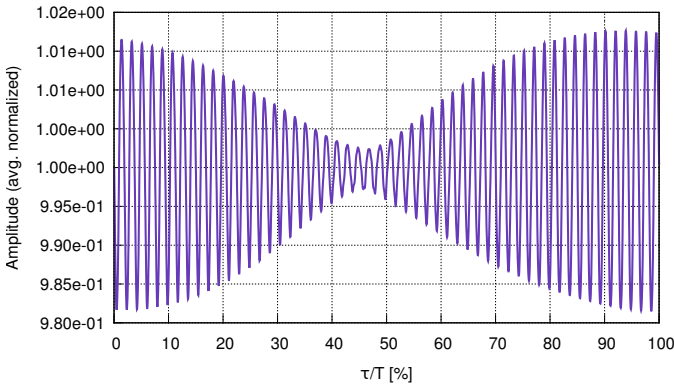


**Figure 7.2:** $F^{TOT}$, Rotor row resulting force

As can be seen, the most relevant contribution to the rotor unsteadiness came from the blade passing frequency of the incoming wakes $(BPF_1)$ and the passage of downstream potential field $(BPF_2)$.

It must be also pointed out that different frequency combinations are clearly visible in the spectrum that is 2BPF1, BPF1+BPF2, 2BPF2 and BPF2-BPF1 with a lower intensity. Since the two most relevant in forcing effects are the ones at the BFPs, a more deeply analysis is requested to well understand the behaviour of the unsteady pressure field.
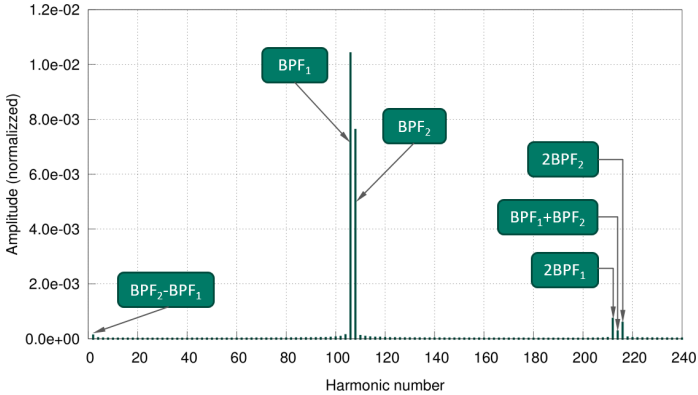


**Figure 7.3:** DFT spectrum of unsteady blade loading

## 7.2 Tyler and Sofrin interaction

Although acoustic emissions in this type of machine are not a main problem, the use of acoustic rules can give useful information about the forcing due to the non-stationary pressure field. Considering individually the stages S1-R and R-S2, the acoustic interaction that may occur can be described using the acoustic formulation proposed by Tyler and Sofrin in [63]. Briefly, referring to BPF1, the main circumferential pressure distortion outgoing from the stator is described by a number of lobes equal to the number of S1 blades. The interaction with the rotor field which exhibits a circumferential distortion with 120 lobes, generates through the wave scattering mechanism, different circumferential distortions with

number of lobes, more properly called circumferential order (*i.e* the number of nodal diameter of the resulting distortion in the frame of reference of the second row) $m_2$, equal to a linear combination according to the relations in 7.4.

$$m_2 = k_1 N_1 - k_2 N_2 \tag{7.4}$$

$$\omega_2 = k_1 N_1 \left( \Omega_1 - \Omega_2 \right) \tag{7.5}$$

Where:

- $N_1, N_2$ blades numbers

- $\Omega_1, \Omega_2$ angular pulsation of the rows

- $k_1$ harmonic index

- $k_2$ scattering index

- $m_2$ circumferential order of scattered wave

- $\omega_2$ pulsation of scattered wave
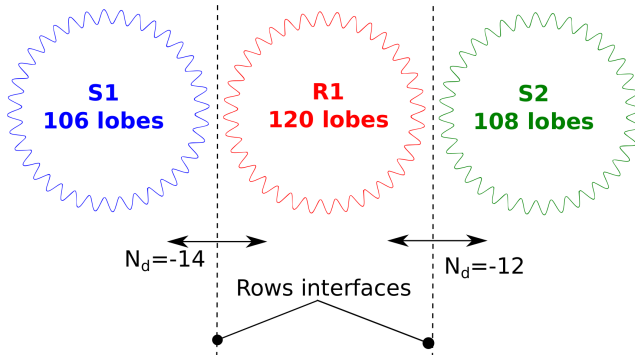


**Figure 7.4:** Stators-Rotor interaction: Acoustic scattering

In the case under investigations, as $m$ in the rotor frame of reference for both upstream and downstream interaction (with $k_1 = 1$ and $k_2 = -1$, usually the strongest interaction)

results negative, the scattered acoustic wave moves in circumferential direction contra-rotating with the rotors, while being the stator obviously fixed, the frequency of the scattered wave is unchanged according to the Eq. 7.5. This is the reason why, in the DFT spectrum stators scattering cannot be identified, yet this study can give useful information on the nodal diameter most excited by this interaction (the ones closest to $m_2$). As last verification, the upstream/downstream incoming acoustic sources and the genesis of scattering waves, can be visualized through the DFT of the whole flow field at the blade passing frequency harmonics as report in Figs. 7.5a and 7.5b.



(a) Upstream interaction



(b) Downstream interaction
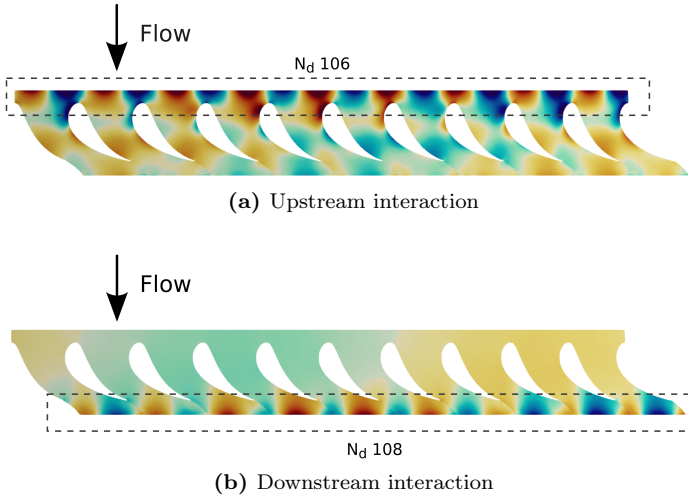
**Figure 7.5:** DFT analysis: Interaction visualizations

# 8

## Aeroelasticity in multi-row environment

*In this final part of the work, the effects of the multirow environment on the rotor damping behaviour are quantified by means of a 1.5 stage unsteady computations with vibrating rotor. The aim of this unconventional and demanding computation is to comfirm the results obtained with single blade classical approach used for aerodynamic damping evaluation.*

## 8.1   Multirow flutter assessments

All flutter analyses for the rotor under investigation have been carried out using a classical setup for flutter analysis which takes into account an isolated row only. This CFD domain it is not completely representative of a row within the turbine, where the mutual unsteady effects of neighbor rows acting on the rotor itself (see [64]). To include these effects, and in particular if the logarithmic decrement is affected by adjacent rows, a non conventional flutter study is performed

in multi-row environment (in Fig. 8.1 an overview on the 1.5 stage CFD domain is reported).

Obviously, due to the inherent unsteady behaviour of the interactions between the vibrating rotor, a comprehensive unsteady simulation is adopted, and so this CFD run is particularly demanding in term of numerical effort and computational time. In this case, the tangential periodicity is set on the whole annulus and then, the advantages obtained by the use of the phase lagged BCs as in chapter 6 and 7 cannot be exploited. This results in a large number of block involved in the computation.
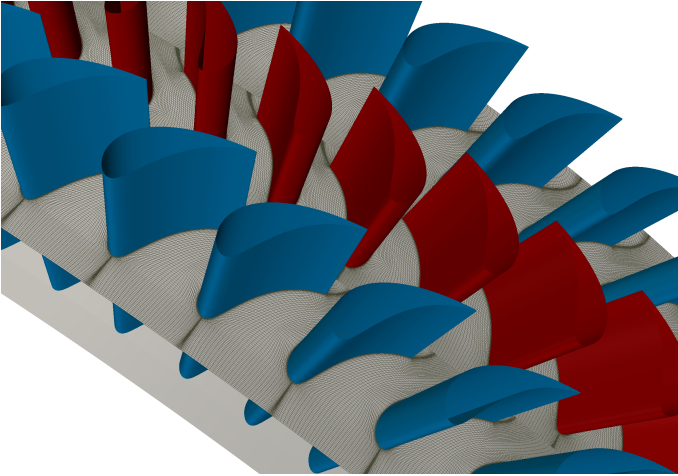


**Figure 8.1:** Overview on the 1.5 stage CFD domain

To evaluate the possible coupling effects between rows interactions and the blade vibration, the main introduced simplification is that the frequency of the modeshape and the rotational frequency must must be equal or at least multiples each other.

This allows the reduction of overall simulation period which include the two unsteady phenomena (blade vibration and

stator/rotor interaction) with an accurate resolution for both of them.

The choice of frequencies to be resolved is directly related to the overall computational time of calculation; Indeed when more than a frequency is included, the total simulation period must be contain an integer number of period of each single frequency. So the choice of unsteady phenomena with multiple frequencies ensure the shorter overall simulation period. The worst case is when the frequencies are closer (see Fig. 8.2).



**(a)** Different frequency
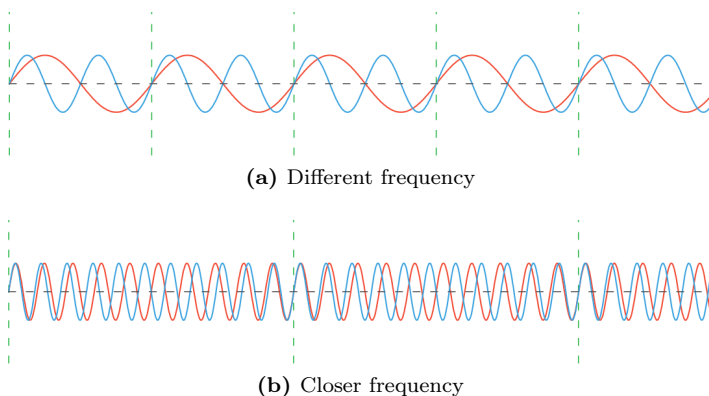


**(b)** Closer frequency

**Figure 8.2:** Effects of closer/different frequency on $n_{per}$

Related to the rows under investigation, none of the modeshapes frequencies found from modal analysis (described in chapter 4) results an exact integer multiple of frequency of rotations even if someone is strictly closer to. It is a well know aspect of the aeroelasticity that a same modeshape alters its damping behaviour if its frequency is changed, yet it is still licit to suppose that a small variation in frequency does not greatly modify the damping behavior of modeshapes. Following this idea the more closer multiple of rotation frequency is searched all over the modeshape families.

### 8.1.1 Aeroelasticity in multirow environment: effect for $N_d = 5$

The more suitable nodal diameter to introduce this concept is the $N_d = 5$ of the first modeshape frequency with a frequency of $f_{Nd_5} = 1076.57 Hz$. The logarithmic decrement curve already seen in chapter 6 is reported in fig. 8.3.
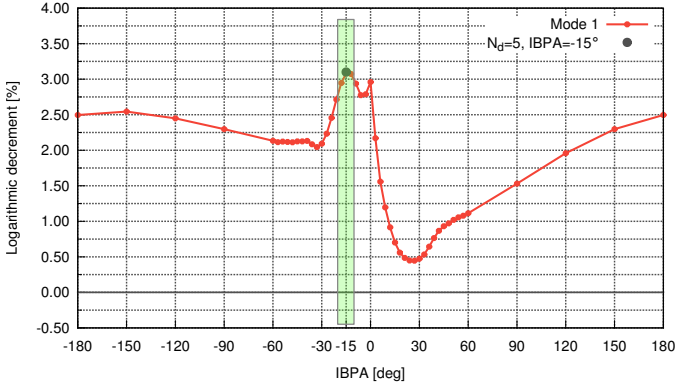


**Figure 8.3:** Mode 1, logarithmic decrement single blade environment

Being $f_R = 60 Hz$ (3600 rpm) the rotational frequency, a small change of $N_d = 5$ modeshapes frequency from $f_{Nd_5}$ to $\widehat{f_{Nd_5}} = 1080 Hz$ allow to obtain multiple frequencies between the two phenomena suitable and so to asses flutter computation in multi-row environment with lower computational time.

$$\frac{\widehat{f_{Nd_5}}}{f_R} = 18 \tag{8.1}$$

From 8.1 it is easy to see that every rotor revolution the blade describes 18 vibrations.

The new altered $\widehat{f_{Nd_5}}$ frequency is different from the original one $f_{Nd_5}$ of 0.32%, (see Fig. 8.4) a deviation such that
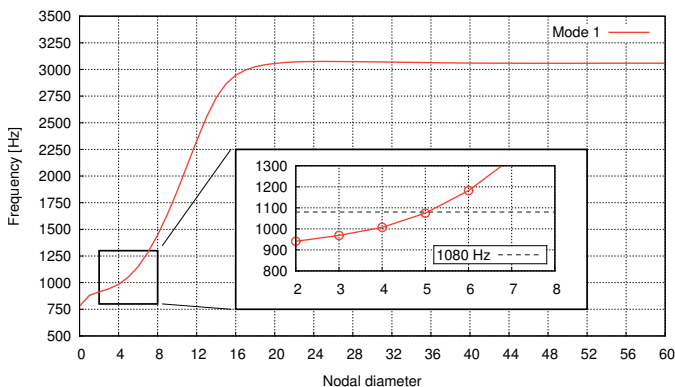
**Figure 8.4:** $N_d$ 5 from $1^{st}$ modeshapes family for multi-row flutter assessments

any differences in the flutter results must be ascribed only to the effects of the multi-row environment and not to the variation in the frequency of the modeshape.

The vibration amplitude which has to be arbitrarily chosen in uncoupled computations for the rotor vibration has been maintained equal to the ones used for the single blade computations described in chapter 6 in order to avoid any flutter discrepancy for computation comparisons. As the rows interaction may be influenced by the secondary flows, the inviscid endwalls approach used for single blade flutter computations could be potentially inadequate. Full Navier-Stokes multirows steady simulation have been already realized in the previous stages of activity (refer to chapters 5 and 7) so it can be used profitably as initialization solution for multirows simulation with vibrating rotor.

This kind of computations are present in this work to validate the single blade approach previously presented, but for the purposes of industrial uses the requests, both in time and computational effort are out of reach. Indeed, the use of full annulus approach require the adoption of a multi-row CFD domain of 334 blocks with a total of about 300M cells.

Due the strong unsteadiness of the 1.5 stage, about 20 periods must be simulate to obtain a convergence in order to well evaluate aeroelastic damping behaviour; this had led to a global computational time of about 415 hours.
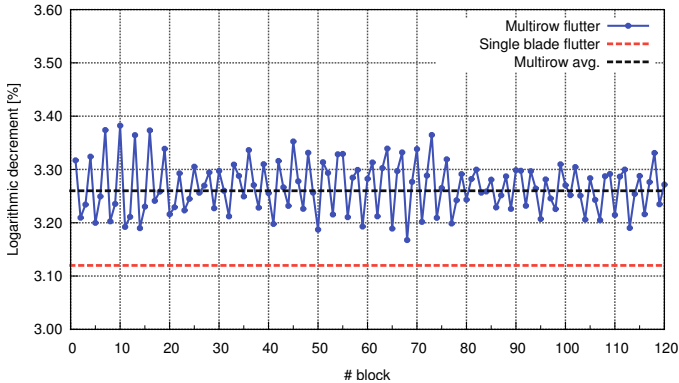


**Figure 8.5:** $N_d = 5$, logarithmic decrement multi-row environment

In Fig. 8.5 the logarithmic decrement for each rotor blade of the CFD domain is reported; every block experiences a different aerodynamic work due to the interaction with the stators. In the same plot, the value of logarithmic decrement resulting for the same modeshape ($N_d = 5$ , $1^{st}$ modeshape family) in single row environment have been reported; as can be seen the damping behaviour of the rotor increases with the multi-row effects as all blocks expects a have a higher logarithmic decrement respect to the single blade flutter computation.

A different value of logarithmic decrement between the two environments is not surprising as the blade is subjected to two quite different unsteady pressure field.

In the single blade case, the only one source of unsteadiness is represented by the vibration of the blade, while in the multi-row computation also the stator/rotor/stator interaction represents a source of unsteadiness. However, the single

|  | Multirow | Isolated row |
|---|---|---|
| Logarithmic decrement | 3.26% | 3.12% |

**Table 8.1:** $N_d = 5, IBPA = -15° : 1^{st}$ modeshape family

blade damping value is not so far from the multi-row one as report in table 8.1; this validates the setup presented in chapter 6 and confirms it as a valid solution to obtain logarithmic decrement values for dynamic analyses of the rows with a higher accuracy.

# 9

# Concluding remarks

Nowadays, in the current energy scenario, one of the parameters that makes a turbomachinery more competitive than another is definitely an high efficiency. This has led to extreme aeromechanical design criteria, favoring the arising of problems related to aeroelastic phenomena. The in-depth study of these phenomena along with the diffusion of numerical methods suitable for simulating them, today allows to look at these types of phenomena not only as an issues, but also to something that can be exploited. In fact, not all kind of blades, faces with the onset of aerodynamic instability, but for high pressure stages such as the one in question, the design is largely flutter-free and therefore with damping behavior.

It is in this perspective that this PhD thesis is framed, that is, to delineate a robust and repeatable strategy to achieve a aeromechanical characterization of rotor blades of high pressure steam turbine stage. With this purposes, the activity proceeds to two parallel branches; on the one hand, the evaluation of the damping effect due to energy exchanges between vibrating blades and fluid, on the other hand the identification of possible aerodynamic source of forcing effects that act on the blade, due to the interactions between adjacent rows.

To meet this objectives, in the first part of the thesis the modal behaviour of the blades is investigated through the use of Open Source tools for FEM analyses, discovering four modeshape family. Due to the strong coupling between blades, all modeshapes results complex modeshapes, with high frequency not common in aeroelasticity area of interest and with the arising of a mode veering between modeshape families. This analyses allow to highlight as the free tools used are fully capable to match the result obtained from a widely used commercial code.

Once the modeshapes are available from modal analyses, the deformation of the aerodynamic surfaces are reproduced on the CFD grid in order to compute the aerodynamic works of the $1^{st}$ harmonic of pressure by means of unsteady simulations. In this phase, to speed up the calculation an inviscid endwall setup is tested compared with the viscid endwalls. The results of this two model are closely in agreement each other in term of logarithmic decrement curves. Neglecting the boundary layer on turbine endwalls the number of cells in spanwise directions have been considerably dropped with a consequent reduction in computational time.

From the analysis of the maps of $1^{st}$ harmonic of pressure emerge as the weird shapes of the logarithmic decrement curves are influenced by several factors: a lower response in pressure for close to zero nodal diameters respect to the others, in a range where modes change swiftly in shape and frequency; also the mode veering of modeshape give its contribution, as highlighted by the assembly of the pseudo-curves of logarithmic decrement.

For the subsequent part of the work, unsteady computation in a 1.5 stage multi-row environment are carried out to investigate the sources of forcing effects on the rotor blades. The interactions of the upstream incoming wakes on the rotor and the passage of the downstream stator potential field with the rotor causes the main forcing effect as arise from the DFT spectrum of unsteady forces on the rotor blades. To pinpoint the contents of this two fundamental harmonics a DFT analyses of the whole CFD domain is performed highlighted as at

the BPFs the acoustic scattered waves could be a low-order forcing according with Tyler and Sofrin theory.

In the last part of the works, a multi-row computation with vibrating blade is performed. The purposes of this computation is to endorse the single blade approach used for aerodynamic damping evaluation due to its prohibitive cost form an industrial point of views, in term of time and computational efforts. This particular run highlight as the multi-row environment alter the damping behaviour of the rows in a positive way (increased logarithmic decrement). Anyway the new value of logarithmic decrement is not so far form the one coming from single blade computations leaving still valid the tuned procedure.

As far as further work is concerned, next steps might go in the following directions:

- *Coupling approach:* This improve the accuracy of the damping prediction due to the mutual interaction between blade and fluid are takes into account.

- *Enhanced setup for multi-row flutter assessments:* A spread overview on the damping behaviour in multi-row environment could be improve the strategy.

# Appendices

# A

# Detail on $k - \omega$ turbulence model

To solve the flowfield, the Navier-Stokes equations are integrated in the RANS formulation on the computational grid, together with the ideal gas and heat transmission equations.

For a turbulent flow the effective fluid viscosity $\mu$ is split up in a laminar part $\mu_l$ and a turbulent eddy viscosity $\mu_t$ as in Eq. A.1.

$$\mu = \mu_l + \mu_t \tag{A.1}$$

The laminar viscosity is a function of the thermal state of the fluid, while a dedicated turbulence models must be used for the calculation of the turbulent viscosity,.

The k–omega ($k - \omega$) turbulence model [65] is a one of the wide used two-equation model which allows to mathematically close the integration of RANS equations.

It includes two extra transport equations; the first transported quantity is the turbulent kinetic energy $k$ and the second is $\omega$, the specific dissipation rate of the turbulence kinetic energy $k$; while the transport variable $k$ determines the energy in turbulence, $\omega$ determines the scale of turbulence.

The model attempts to assess turbulence through two partial differential equations; one for $k$ (see Eq. A.2) and one for

$\omega$ (see Eq. A.3) capable to take into account convection and diffusion of turbulent kinetic energy $k$ and dissipation rate $\omega$.

$$\frac{\partial \rho k}{\partial t} + u_j \frac{\partial \rho k}{\partial x_j} = P_k - \beta^* \rho k \omega + \frac{\partial}{\partial x_j} \left[ (\mu + \sigma^* \mu_t) \frac{\partial k}{\partial x_j} \right] \quad \text{(A.2)}$$

$$\frac{\partial \rho \omega}{\partial t} + u_j \frac{\partial \rho \omega}{\partial x_j} = \alpha \frac{\omega}{k} P_k - \beta \rho \omega^2 + \frac{\partial}{\partial x_j} \left[ (\mu + \sigma \mu_t) \frac{\partial \omega}{\partial x_j} \right] \quad \text{(A.3)}$$

with $\alpha$, $\beta$, $\beta^*$, $\sigma$ and $\sigma^*$ calibration coefficients of the model as in table A.1.

| $\alpha$ | $\beta$ | $\beta^*$ | $\sigma$ | $\sigma^*$ |
|---|---|---|---|---|
| 5/9 | 0.075 | 0.09 | 0.5 | 0.5 |

**Table A.1:** $k - \omega$ calibration coefficients

Once the evolution of $k$ and $\omega$ is established, the eddy viscosity is given by:

$$\mu_t = \rho \frac{k}{\omega} \quad \text{(A.4)}$$

With Stokesian flow hypothesis, the second order stress tensor is expressed through the relation A.5.

$$\tau_{ij} = \mu_t \left[ \frac{\partial u_i}{\partial x_j} + \frac{\partial u_j}{\partial x_i} - \frac{2}{3} \frac{\partial u_k}{\partial x_k} \delta_{ij} \right] - \frac{2}{3} \rho k \delta_{ij} \quad \text{(A.5)}$$

and then the production term $P_k$ of A.2 and A.3 is computed as

$$P_k = \tau_{ij} \frac{\partial u_i}{\partial x_j} \quad \text{(A.6)}$$

The term of production thus defined leads to a non-physical production of turbulence in the stagnation points; to fix it, the correction proposed by Durbin is adopted [66].

$$\mu_t = \rho \frac{k}{\omega_{min}} \tag{A.7}$$

with

$$\omega_{min} = \frac{1}{\mathcal{T}_{tu}} \tag{A.8}$$

where $\mathcal{T}_{tu}$ is the turbulent time scale.

The thermal conductibility of the fluid is is subsequently determined by laminar Prandtl number and turbulent Prandtl number according to eq. A.9.

$$K_t = c_p \left( \frac{\mu_l}{Pr} + \frac{\mu_t}{Pr_t} \right) \tag{A.9}$$

# $\mathcal{B}$
# Flutter computations: Mode 2

In this appendix the logarithmic decrement curve for mode 2 is reported in Fig. B.1 in addition with the relative curves of aerodynamic work and blade average kinetic energy in Fig. B.1. Later the amplitude and phase of the $1^{st}$ harmonic of pressure of representatives outer/inner IBPAs whas show in Fig. B.3 and summarized in the colormap reported in B.4
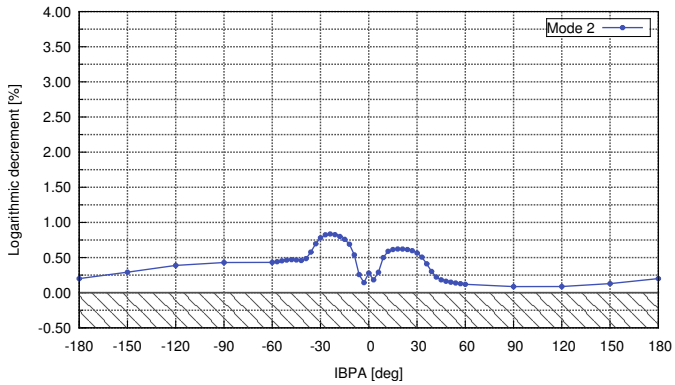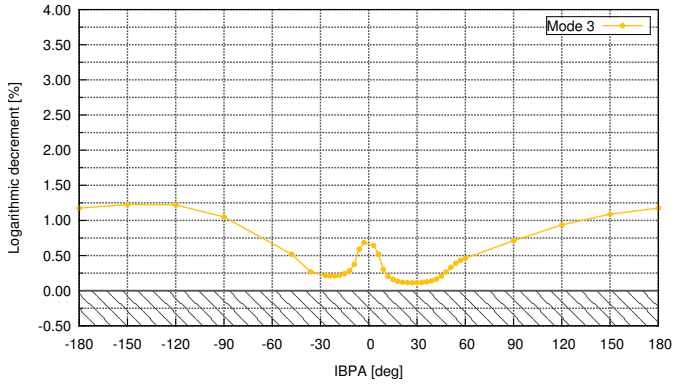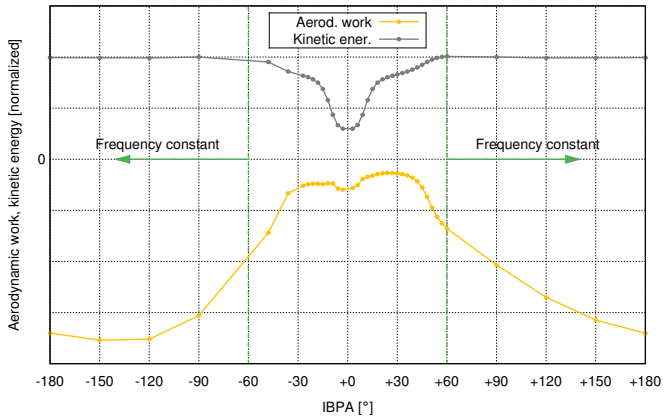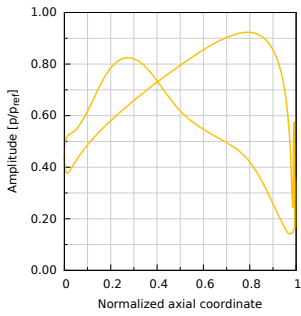
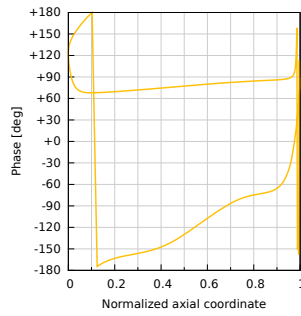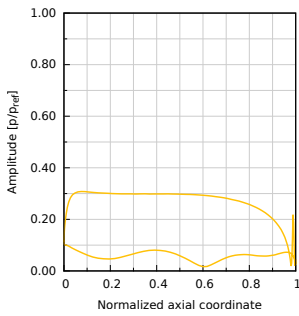**Figure B.1:** Mode 2: Logarithmic decrement curve
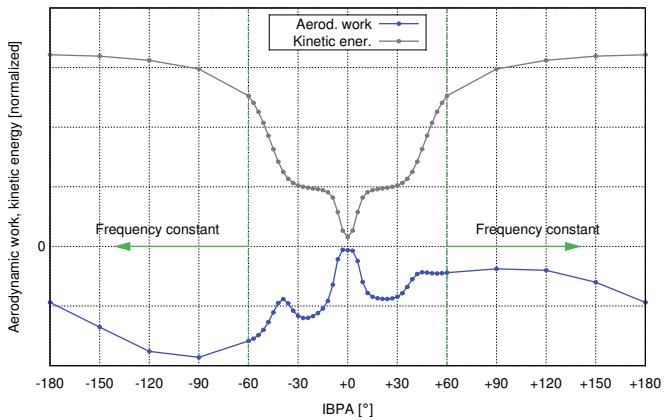


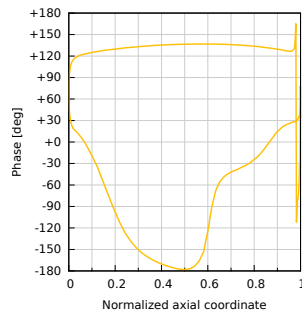**Figure B.2:** Mode 2: Aerodynamic work and blade average kinetic energy
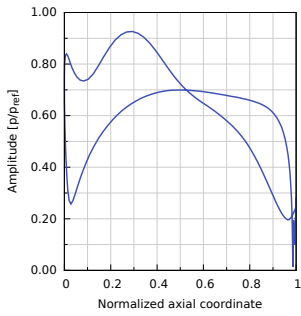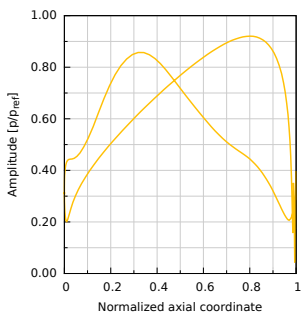
**(a)** IBPA -150, amplitude
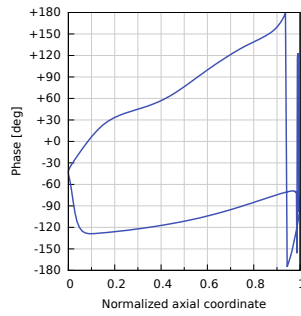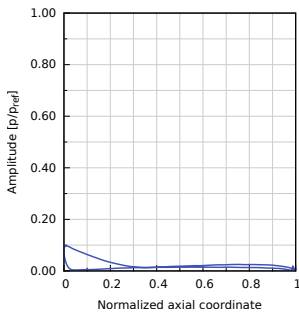
**(b)** IBPA -150, phase
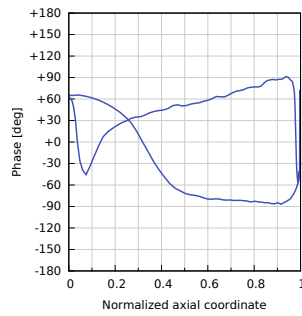
**(c)** IBPA 0, amplitude

**(d)** IBPA 0, phase
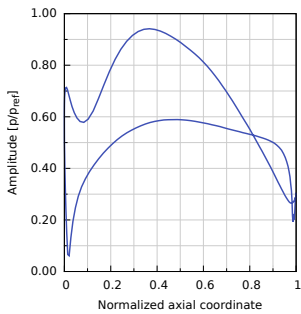
**(e)** IBPA +150, amplitude
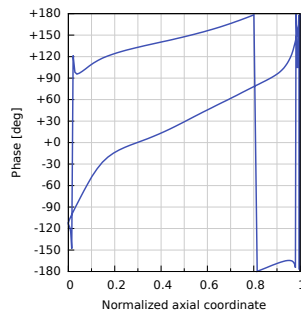
**(f)** IBPA +150, phase

**Figure B.3:** Mode 2, $1^{st}$ harmonic of pressure
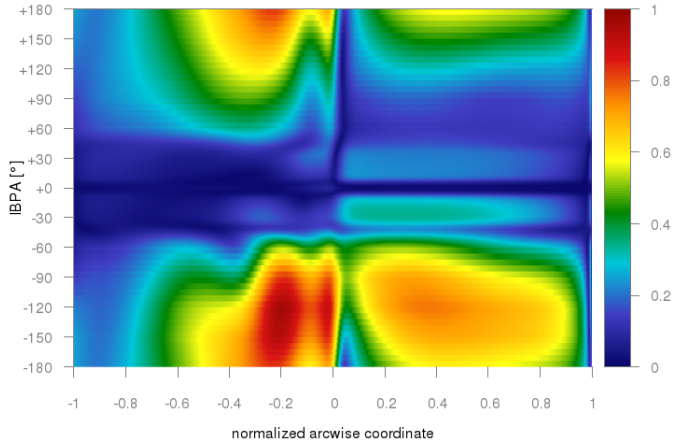
**(a)** Amplitude
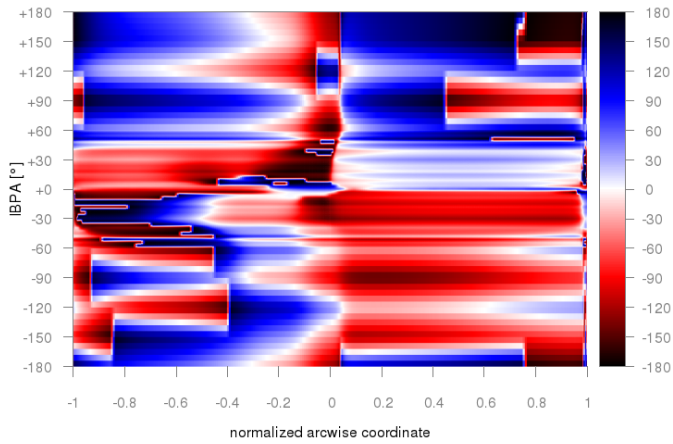


**(b)** Phase

**Figure B.4:** Mode 2, $1^{st}$ harmonic of pressure maps

# $C$
# Flutter computations: Mode 3

In this appendix the logarithmic decrement curve for mode 3 is reported in Fig. C.1 in addition with the relative curves of aerodynamic work and blade average kinetic energy in Fig. C.1. Later the amplitude and phase of the $1^{st}$ harmonic of pressure of representatives outer/inner IBPAs whas show in Fig. C.3 and summarized in the colormap reported in C.4

**Figure C.1:** Mode 3: Logarithmic decrement curve



**Figure C.2:** Mode 3: Aerodynamic work and blade average kinetic energy

**(a)** IBPA -150, amplitude

**(b)** IBPA -150, phase

**(c)** IBPA 0, amplitude

**(d)** IBPA 0, phase

**(e)** IBPA +150, amplitude
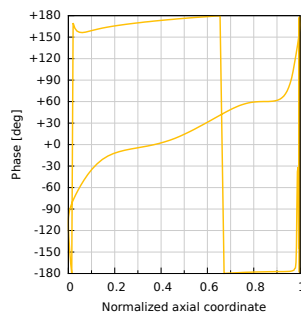
**(f)** IBPA +150, phase

**Figure C.3:** Mode 3, $1^{st}$ harmonic of pressure
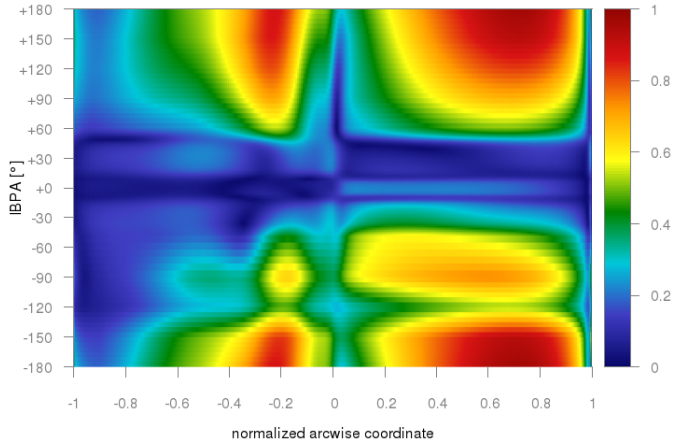
**(a)** Amplitude
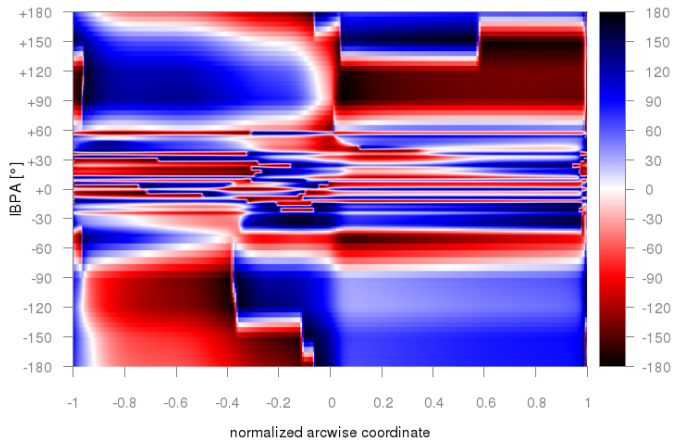


**(b)** Phase

**Figure C.4:** Mode 3, $1^{st}$ harmonic of pressure maps

# $\mathcal{D}$
# Flutter computations: Mode 4

In this appendix the logarithmic decrement curve for mode 3 is reported in Fig. D.1 in addition with the relative curves of aerodynamic work and blade average kinetic energy in Fig. D.1. Later the amplitude and phase of the $1^{st}$ harmonic of pressure of representatives outer/inner IBPAs whas show in Fig. D.3 and summarized in the colormap reported in D.4
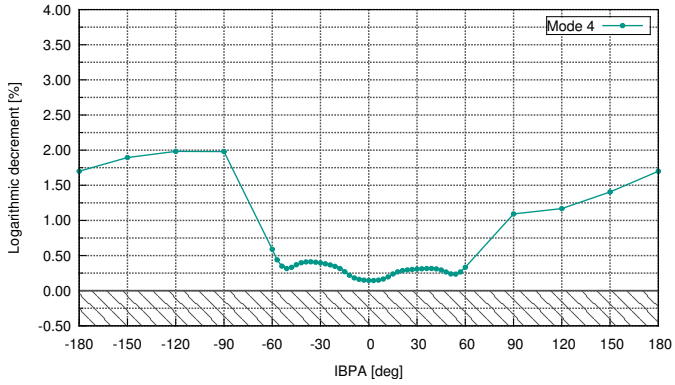
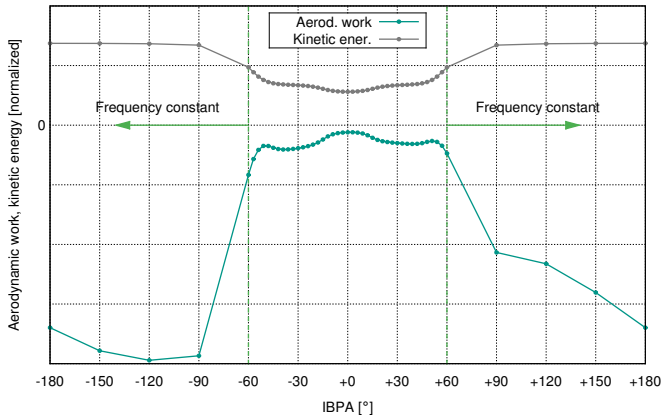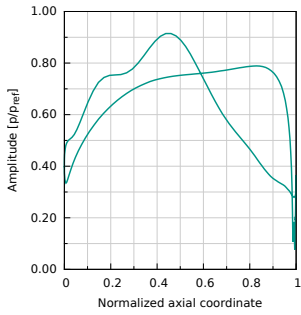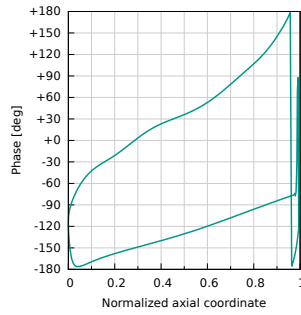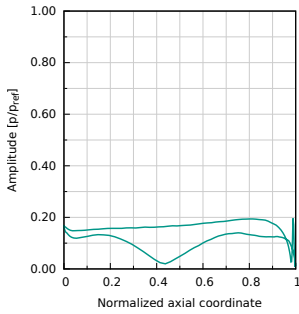**Figure D.1:** Mode 4: Logarithmic decrement curve



**Figure D.2:** Mode 4: Aerodynamic work and blade average kinetic energy

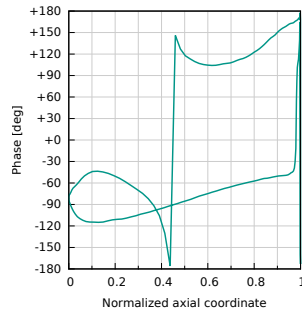**(a)** IBPA -150, amplitude



**(b)** IBPA -150, phase



**(c)** IBPA 0, amplitude



**(d)** IBPA 0, phase
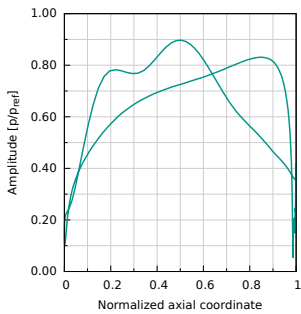


**(e)** IBPA +150, amplitude
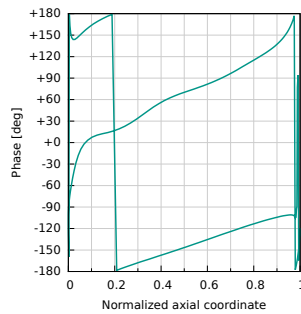


**(f)** IBPA +150, phase

**Figure D.3:** Mode 4, $1^{st}$ harmonic of pressure
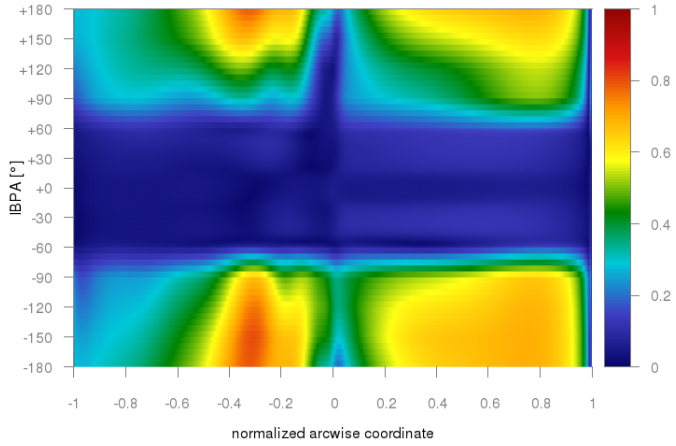
**(a)** Amplitude
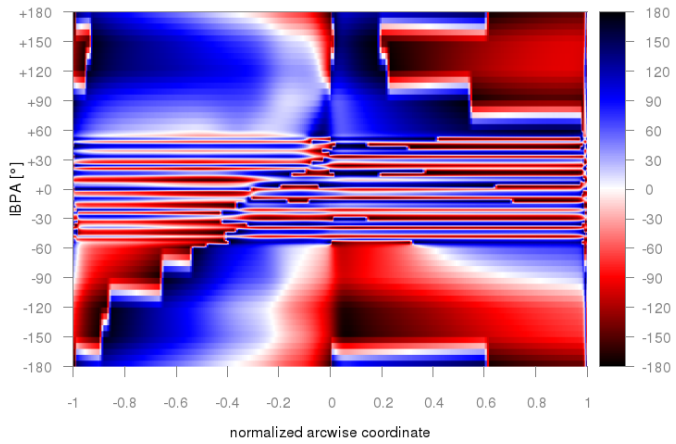


**(b)** Phase

**Figure D.4:** Mode 4, $1^{st}$ harmonic of pressure maps

$\mathcal{E}$

# Rotor forces

In the following plots the contributes tangential $F_T$, axial $F_X$, and radial $F_R$ of $F^{TOT}$ are reported as percentage of the period of the simulation.
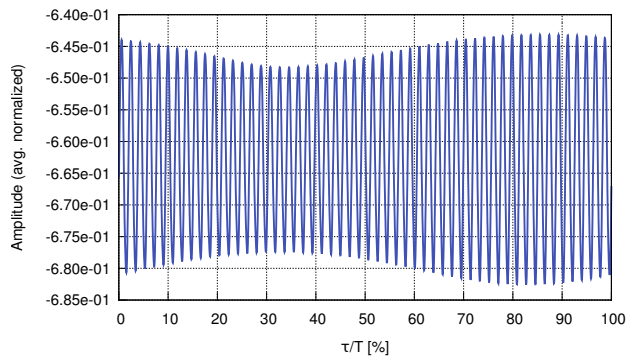
(a) $F_T$, Tangential force
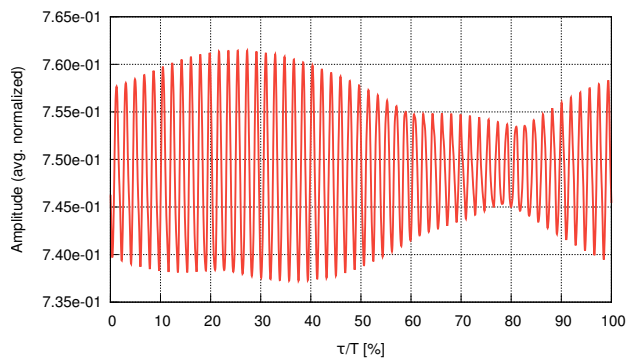


(b) $F_X$, Axial force
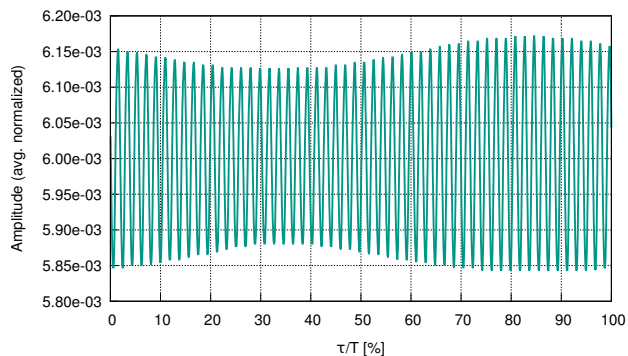


(c) $F_R$, Radial force

**Figure E.1:** Unsteady force on rotor row

# Bibliography

[1] L. Pinelli, F. Poli, A. Arnone, and C. Schipani. A time-accurate 3D method for turbomachinery blade flutter analysis. In $12^{th}$ *International Symposium on Unsteady Aerodynamics, Aeroacoustics and Aeroelasticity of Turbomachines (ISUAAAT)*, 2009. September 1–4, London, UK, paper I12-S8-3.

[2] Achim Zanker, Peter Ott, and Paolo Calza. Experimental aeroelastic investigation of vibrating turbine blade clusters. In *10th European Conference on Turbomachinery*, number EPFL-CONF-186098, pages 210–221. Lappeenranta University of Technology, 2013.

[3] F. Vanti, L. Pinelli, F. Poli, and A. Arnone. Aeroelastic investigation of turbine blade assemblies: Cluster system and mistuned rows. *European Conference on Turbomachinery Fluid dynamics and Thermodynamics*, 2017. April 3-7, Stockholm, Sweden, Paper ETC2017-144.

[4] B. Lakshminarayana. *Fluid Dynamics and Heat Transfer of Turbomachinery*. Wiley-Interscience publication. John Wiley & Sons.

[5] CH Sieverding. Recent progress in the understanding of basic aspects of secondary flows in turbine blade passages. *Journal of Engineering for Gas Turbines and Power*, 107(2):248–257, 1985.

[6] K Takeishi, M Matsuura, S Aoki, and T Sato. An experimental study of heat transfer and film cooling on low aspect ratio turbine nozzles. In *ASME 1989 International Gas Turbine and Aeroengine Congress and Exposition*, pages V004T08A021–V004T08A021. American Society of Mechanical Engineers, 1989.

[7] Sumanta Acharya and GI Mahmood. Turbine blade aerodynamics. *The Gas Turbine Handbook*, 1:364–380, 2006.

[8] DG Ainley and G Cr Mathieson. A method of performance estimation for axial-flow turbines. Technical report, aeronautical research council London (United Kingdom), 1951.

[9] HRM Craig and HJA Cox. Performance estimation of axial flow turbines. *Proceedings of the Institution of Mechanical Engineers*, 185(1):407–424, 1970.

[10] SC Kacker and U Okapuu. A mean line prediction method for axial flow turbine efficiency. *Journal of engineering for power*, 104(1):111–119, 1982.

[11] M Govardhan, N Venkatrayulu, and D Prithvi Raj. Investigations into secondary losses of a turbine nozzle cascade. In *Eighth Australasian Fluid Mechanics Conference: proceedings, Newcastle, New South Wales, 28 November-2 December, 1983;[organising committee, RA Antonia... et al.].*, volume 1. University of Newcastle, 1983.

[12] S.L. Dixon. *Fluid Mechanics and Thermodynamics of Turbomachinery*. Elsevier Science, 2005.

[13] R.H. Aungier. *Turbine Aerodynamics: Axial-flow and Radial-inflow Turbine Design and Analysis*. ASME Press, 2006.

[14] R Parker and J F. Watson. Interaction effects between blade rows in turbomachines. 186:331–340, 06 1972.

[15] Colin Osborne. Compressible unsteady interactions between blade rows. *AIAA Journal*, 11(3):340–346, 1973.

[16] Z. Zou, S. Wang, H. Liu, and W. Zhang. *Axial Turbine Aerodynamics for Aero-engines: Flow Analysis and Aerodynamics Design*. Springer Singapore, 2018.

[17] J. Verdon. Linearized unsteady aerodynamic theory. *In AGARD Manual on Aeroelasticity in Axial Flow in Turbomachines*, AGARD-AG-298, 1987.

[18] D. Whitehead. Classical two-dimensionnal methods. *In AGARD Manual on Aeroelasticity in Axial Flow in Turbomachines*, AGARD-AG-298, 1987.

[19] K.C. Hall and W.S. Clark. Linearized Euler predictions of unsteady aerodynamic loads in cascades. *AIAA Journal*, 31:540–550, 1993.

[20] K.C. Hall and C.B. Lorence. Calculation of three-dimensional unsteady flows in turbomachinery using the linearized harmonic Euler equations. *Transactions of the ASME, Journal of turbomachinery*, 115:800–809, 1993.

[21] J.C. Chassaing and G. Gerolymos. Compressor flutter analysis using time-nonlinear and time-linearized 3-d navier-stokes methods. In $9^{th}$ *International Symposium on Unsteady Aerodynamics, Aeroacoustics and Aeroelasticity of Turbomachines*, 2000.

[22] A. Arnone, F. Poli, and C. Schipani. A method to assess flutter stability of complex modes. In $10^{th}$ *International Symposium on Unsteady Aerodynamics, Aeroacoustics and Aeroelasticity of Turbomachines*, 2003.

[23] F. Poli, E. Gambini, A. Arnone, F. Poli, and C. Schipani. A 3d time-linearized method for turbomachinery blade flutter analysis. In $11^{th}$ *International Symposium on Unsteady Aerodynamics, Aeroacoustics and Aeroelasticity of Turbomachines*, 2006.

[24] V. Chenaux and B. Grueber. Aeroelastic investigation of an annular transonic compressor cascade: Numerical sensitivity study for validation purposes. 2015. ASME Turbo Expo, June 15–19, Montreal, Canada.

[25] I. McBean, F. Liu, K. Hourigan, and M. Thompson. Simulations of aeroelasticity in an annular cascade using a parallel 3-dimensional Navier-Stokes solver. *ASME paper GT–2002–30366*, 2002. ASME Turbo Expo, June 3–6, Amsterdam, The Netherlands.

[26] I. McBean, K. Hourigan, M. Thompson, and F. Liu. Prediction of flutter of turbine blades in a transonic annular cascade. *ASME Journal of Fluid Engineering*, 127:1053–1058, November 2005.

[27] M. Vahdati, A. Sayma, and M. Imregun. Case studies in turbomachinery aeroelasticity using an integrated 3D non-linear method. In *Lecture series programme on Aeroelasticity in axial flow turbomachines*. Von Karman Institute for fluid dynamics, May 1999.

[28] H. Doi and J. Alonso. Fluid/structure coupled aeroelastic computations for transonic flows in turbomachinery. *ASME paper GT–2002–30313*, 2002. ASME Turbo Expo, June 3–6, Amsterdam, The Netherlands.

[29] P. Cinnella and P. De Palma. A numerical method for turbomachinery aeroelasticity. *Transactions of the ASME, Journal of turbomachinery*, 126:310–316, 2004.

[30] L. Pinelli, F. Poli, J. Bellucci, Matteo Giovannini, and A. Arnone. Evaluation of fast numerical methods for turbomachineryblade flutter analysis. In $14^{th}$ *International Symposium on Unsteady Aerodynamics, Aeroacoustics and Aeroelasticity of Turbomachines*, 2015.

[31] Dan Su, Weiwei Zhang, Mingsheng Ma, and Zhengyin Ye. An efficient coupled method of cascade flutter investigation based on reduced order model. 07 2013.

[32] Yun ZHENG and Hui YANG. Coupled fluid-structure flutter analysis of a transonic fan. *Chinese Journal of Aeronautics*, 24(3):258 – 264, 2011.

[33] Peter D Silkowski, Chae M Rhie, George S Copeland, James A Eley, and James M Bleeg. Computational-fluid-dynamics investigation of aeromechanics. *Journal of propulsion and power*, 18(4):788–796, 2002.

[34] R Srivastava, MA Bakhle, TG Keith, and GL Stefko. Flutter analysis of a transonic fan. In *ASME Turbo Expo 2002: Power for Land, Sea, and Air*, pages 837–844. American Society of Mechanical Engineers, 2002.

[35] Hongsik Im, Xiangying Chen, and Gecheng Zha. Detached eddy simulation of transonic rotor stall flutter using a fully coupled fluid-structure interaction. In *ASME 2011 Turbo Expo: Turbine Technical Conference and Exposition*, pages 1217–1230. American Society of Mechanical Engineers, 2011.

[36] S Moffatt and L He. On decoupled and fully-coupled methods for blade forced response prediction. *Journal of fluids and structures*, 20(2):217–234, 2005.

[37] T.H. Fransson. Basic introduction to aeroelasticity. In *Lecture series programme on Aeroelasticity in axial flow turbomachines*. Von Karman Institute for fluid dynamics, May 1999.

[38] D. Vogt. *Experimental investigation of three-dimensional mechanisms in low-pressure turbine flutter*. PhD thesis, Kungla Tekniska Höegskolan, 2005.

[39] T.H. Fransson. Dynamic aeroelasticity. In *Lecture series programme on Aeroelasticity in axial flow turbomachines*. Von Karman Institute for fluid dynamics, May 1999.

[40] K.C. Hall. Linearized unsteady aerodynamics. In *Lecture series programme on Aeroelasticity in axial flow turbomachines*. Von Karman Institute for fluid dynamics, May 1999.

[41] F. Poli. Sviluppo di un risolutore per lo studio dei fenomeni aeroelastici nelle palettature di turbomacchine. Tesi di laurea in ingegneria meccanica, Università degli Studi di Firenze, Luglio 2001.

[42] I. McBean, F. Liu, K. Hourigan, and M. Thompson. Simulations of aeroelasticity in an annular cascade using a parallel 3-dimensional Navier-Stokes solver. *ASME paper GT–2002–30366*, 2002. ASME Turbo Expo, June 3–6, Amsterdam, The Netherlands.

[43] I. McBean, K. Hourigan, M. Thompson, and F. Liu. Prediction of flutter of turbine blades in a transonic annular cascade. *ASME Journal of Fluid Engineering*, 127:1053–1058, November 2005.

[44] A. Arnone. Viscous analysis of three-dimensional rotor flow using a multigrid method. *Journal of turbomachinery*, 116:435–445, 1994.

[45] A. Arnone, M-S. Liou, and L.A. Povinelli. Multigrid calculation of three-dimensional viscous cascade flows. *Journal of propulsion and power*, 9(4):605–614, 1993.

[46] Antony Jameson. Time dependent calculations using multigrid, with applications to unsteady flows past airfoils and wings. *AIAA paper*, 1596:1991, 1991.

[47] Andrea Arnone and Roberto Pacciani. Rotor-stator interaction analysis using the navier-stokes equations and a multigrid method. In *ASME 1995 International Gas Turbine and Aeroengine Congress and Exposition*, pages V001T01A041–V001T01A041. American Society of Mechanical Engineers, 1995.

[48] Antony Jameson. Numerical solution of the euler equations for compressible inviscid fluids. *Numerical methods for the Euler equations of Fluid Dynamics*, 1, 1985.

[49] Eli Turkel. Improving the accuracy of central difference schemes. In *11th International Conference on Numerical Methods in Fluid Dynamics*, pages 586–591. Springer, 1989.

[50] RC Swanson and Eli Turkel. Artificial dissipation mid cehtral dipferfnce sceemes for tee ewr and uavier-stokes equations. 1987.

[51] Luigi Martinelli and Antony Jameson. *Validation of a multigrid method for the Reynolds averaged equations*. American Institute of Aeronautics and Astronautics, 1988.

[52] D. C. Wilcox. Formulation of the $k-\omega$ turbulence model revisited. 46(11):2823–2838, November 2008.

[53] T.H. Fransson and J.M. Verdon. Updated report on "standard configurations for unsteady flow through vibrating axial-flow turbomachine-cascades", July 1991.

[54] Standard configurations for unsteady flow through vibrating axial-flow turbomachine-cascades (stcf). http://www.energy.kth.se/proj/projects/MarkusJoecker/STCF/STCF4_update/stcf4_update.htm, 1991.

[55] Matteo Giovannini. *Development of a Phase-Lagged approach for unsteady turbomachinery analysis*. PhD thesis, University of Florence, Italy, 2012.

[56] GA Gerolymos and Vincent Chapin. Generalized expression of chorochronic periodicity in turbomachinery blade-row interaction. *La Recherche Aerospatiale*, (5):69–73, 1991.

[57] Francesco Poli. *Development of a time-linearized computational method with application to bladerow aeroelasticity.* PhD thesis, University of Florence, Italy, 2004.

[58] Arthur W. Leissa. On a curve veering aberration. *Zeitschrift für angewandte Mathematik und Physik ZAMP*, 25(1), Jan 1974.

[59] F. Rubechini, M. Marconcini, A. Arnone, S. Cecchi, and F. Daccà. Some aspects of cfd modeling in the analysis of a low-pressure steam turbine. In *ASME Turbo Expo, 14-17 May, Montreal, Canada*, number GT2007-27235, 2007.

[60] F. Rubechini, A. Schneider, A. Arnone, S. Cecchi, and P. Garibaldi. A redesign strategy to improve the efficiency of a 17-stage steam turbine. 134(3):031021, 2012.

[61] W. F. McGreeham and S. H. Ko. Power dissipation in smooth and honeycomb labyrinth seals. In *ASME Turbo Expo, 5-8 June, Toronto, Canada*, number 89-GT-220, 1989.

[62] Lorenzo Peruzzi, Juri Bellucci, Lorenzo Pinelli, Andrea Arnone, Lorenzo Arcangeli, Lorenzo Cosi, and Marco Mazzucco. Numerical aerodynamic damping evaluation of high-pressure steam turbine blades for aeromechanical characterization. In *ASME Turbo Expo 2016: Turbomachinery Technical Conference and Exposition*, pages V008T26A012–V008T26A012. American Society of Mechanical Engineers, 2016.

[63] John M Tyler and Thomas G Sofrin. Axial flow compressor noise studies. Technical report, SAE Technical Paper, 1962.

[64] Kwen Hsu, Dan Hoyniak, and MS Anand. Full-annulus multi-row flutter analyses. In *Proceedings of ASME Turbo Expo 2014: Turbine Technical Conference and Exposition*, pages 1453–1462, 2012.

[65] D.C. Wilcox. *Turbulence modeling for CFD*. DCW Industries, 1998.

[66] PA Durbin. On the k-3 stagnation point anomaly. *International journal of heat and fluid flow*, 17(1):89–90, 1996.